A discontinuous Galerkin method for nonlinear shear-flexible shells

Brandon L. Talamini[a], Raúl A. Radovitzky[a,*]

[a] *Department of Aeronautics and Astronautics*
Massachusetts Institute of Technology
Cambridge, MA 02139

Abstract

In this paper, a discontinuous Galerkin method for a nonlinear shear-flexible shell theory is proposed that is suitable for both thick and thin shell analysis. The proposed method extends recent work on Reissner-Mindlin plates to avoid locking without the use of projection operators, such as mixed methods or reduced integration techniques. Instead, the flexibility inherent to discontinuous Galerkin methods in the choice of approximation spaces is exploited to satisfy the thin plate compatibility conditions a priori. A benefit of this approach is that only generalized displacements appear as unknowns. We take advantage of this to craft the method in terms of a discrete energy minimization principle, thereby restoring the Rayleigh-Ritz approach. In addition to providing a straightforward and elegant derivation of the discrete equilibrium equations, the variational character of the method could afford numerous advantages in terms of mesh adaptation and available solution techniques. The proposed method is exercised on a set of benchmarks and example problems to assess its performance numerically, and to test for shear and membrane locking.

Keywords: shells, discontinuous Galerkin, locking, variational

1. Introduction

Shell structures are perhaps the most challenging setting for numerical analysis in solid mechanics. The primary difficulty encountered is *locking*, wherein the approximation power of the numerical method diminishes as the shell thickness is reduced. The problem is similar to that faced in nearly incompressible elasticity. Shear-flexible shell theories are generally formulated with two kinematic fields: the displacement of the shell mid-surface, and some representation of the rotation of fibers originally transverse to the shell surface. The root of the locking problem is that when standard finite element interpolations are used for both fields, the pair of approximations spaces taken together do not represent the thin-shell limit well. In particular, this incompatibility prevents the transverse shear strains from vanishing, leading to spurious shear energy. The problem is exacerbated as the shell thickness t tends to zero, since the bending energy is smaller than the transverse shear energy by a factor of t^2, and the spurious shear energy caused by the incompatibility of the discrete function spaces becomes dominant.

The goal for numerical analysis of shear-flexible plates and shells is a method that converges uniformly with respect to the thickness, while remaining simple. These requests are somewhat antagonistic, and the search for acceptable compromises has generated a large body of literature (see the review by [1] and the references therein). Most approaches operate on the shear energy by replacing the rotations in the shear strain term with some lower order projection. There are two main techniques applied to effect this projection: one avenue followed has been mixed methods, in which the shear strain is added as an unknown, such as [2, 3, 4, 5, 6] for Reissner-Mindlin plates, and the well-known MITC elements [7, 8, 9] that extend this idea to curved shells. The other main approach, popular in commercial finite element codes, is to use a reduced

*Corresponding author.
Email addresses: talamini@mit.edu (B. L. Talamini), rapa@mit.edu (R. A. Radovitzky)

integration rule [10, 11, 12] with some suitable stabilization of the attendant rank deficiency [13, 14, 15]. Both approaches have drawbacks: for mixed methods, the energy minimum problem is transformed into a saddle point, which leads to indefinite stiffness matrices that are more difficult to invert. From the perspective of formulation, mixed method elements must satisfy the Babuška-Brezzi (inf-sup) condition to be convergent, and proving this for any element is not a simple task [16, 17, 6]. On the other hand, reduced integration methods are simple to formulate and to implement, but are ad hoc, without rigorous stability and accuracy guarantees.[1] Furthermore, it can sometimes be difficult to detect when hourglass modes are excited in complex engineering problems (e.g. high-rate dynamic problems with nonlinear constitutive behavior), which can make the use of under-integrated elements unsafe.

The development of discontinuous Galerkin (DG) finite element methods has provided new means to attack locking problems, as evidenced by the formulations in [19, 20, 21] for nearly and fully incompressible elasticity and in [22] for Stokes flow. In particular, the last 10 years has seen the development of several locking-free DG methods for Reissner plates [23, 24, 25, 26]. In [24, 25, 26], the flexibility in the choice of the approximation spaces afforded by discontinuous Galerkin methods is exploited to ensure satisfaction of the natural compatibility conditions of the thin plate limit. These families of elements are locking-free without recourse to mixed methods or reduced integration. Notwithstanding these advances for plates, DG methods have barely been explored for the analysis of curved shear-flexible shells. The notable exception is the work of Güzey et al. on linear shells with their *embedded discontinuous Galerkin* method [27, 28].

In this article, the discontinuous Galerkin approach is extended to the nonlinear analysis of finitely deforming, shear-flexible shells. In the proposed method, locking is alleviated without a projection operator by extending the compatibility strategy of Arnold et al. [24] to shells. An advantage of this approach is that locking is avoided without the introduction of generalized force unknowns. This paves the way to casting the method in terms of a minimum principle. To this end, a discrete potential energy functional is proposed, as in the DG method of Ten Eyck and Lew for nonlinear elasticity [20] (also related are the DG elasticity methods in [29, 30] derived from three-field mixed variational principles). The discrete equilibrium equations follow as the first variation of this functional, which furnishes an elegant means to derive the method. The variational structure also confers numerous benefits. Symmetry of the bilinear form and hence the stiffness matrix is guaranteed, since it is the second variation of a scalar potential, which is always symmetric. The tools of mathematical optimization may be brought to bear for solution, including powerful existing software libraries. The energy principle also provides a physically meaningful basis for error estimation for mesh adaptation that applies even in nonlinear problems, in which there is no natural norm [31, 32, 33]. It is worth noting that discontinuous Galerkin methods are particularly well-suited to *hp*-adaptation.

The structure of this paper is as follows. A review of the adopted shell theory, the classical directed surface theory in the form developed by Simo and Fox [34], is given in Section 2. In Section 3, the new nonlinear DG shell method is proposed. (In addition, the linearized kinematics version is provided for the purposes of making normed error measurements and applying linear benchmarks in the next section). As in any discontinuous Galerkin method, a key step is the projection of the derivative operator, sometimes called the *DG derivative*. The character of the shell as a two dimensional surface embedded in three dimensional space merits special attention; accordingly, a full derivation of this operator is given in Section 3.4. In Section 4, details of an implementation strategy are provided to promote adoption of the proposed method and further development. This includes the computation and storage strategy of the DG derivative. Explicit forms of the nodal forces are provided. (Explicit forms of the element stiffness matrices are additionally provided in Appendix A). Numerical studies are presented in Section 5 as a preliminary assessment of the performance of the proposed method and to test for locking. These tests indicate that the method is promising as an analysis tool for both thick and thin shells.

Throughout the paper, the notation of Simo and Fox [34] is largely used. Scalar quantities are indicated by italic type, and vectors (in $\mathbb{R}^3$) are written in boldface type. Lower-case Greek letters are used to index two-dimensional tensor components, while lower-case Roman letters will be reserved for three dimensional

[1] Under some restrictions, reduced integration approaches are equivalent to mixed methods [18, 12]. However, this equivalence breaks down under nonlinear or anisotropic material behavior.

components. A tensor index appearing twice in the same term implies summation over the range of the index.

2. Shell formulation

The adopted shell formulation is that of a classical single director Cosserat surface, in the form developed by Simo and Fox [34]. For completeness, and to fix notation, the theory is summarized in this section.

2.1. Kinematics

The parameterization of the shell mid-surface $\mathcal{S}$ is given by an injective map $\boldsymbol{\varphi} : \mathcal{A} \subset \mathbb{R}^2 \to \mathbb{R}^3$.[2] The mid-surface is assumed to be orientable and compact, with the boundary indicated by $\partial\mathcal{S}$. Material points in the shell body are located relative to the mid-surface with the director vector field $\mathbf{t} : \mathcal{A} \to S^2$, where S^2 is the unit sphere. The basic kinematic assumption of the theory is that points in the current placement of the shell body $\mathcal{B} = \mathcal{S} \times (c^-, c^+)$ are given by

$$\mathbf{x} = \boldsymbol{\Phi}(\xi^1, \xi^2, \xi^3) := \boldsymbol{\varphi}(\xi^1, \xi^2) + \xi^3 \mathbf{t}(\xi^1, \xi^2), \quad \xi^3 \in (c^-, c^+) \tag{1}$$

where $t := c^+ - c^-$ is the thickness of the shell.

The reference configuration is taken to be the undeformed shell, which possesses its own mid-surface map $\boldsymbol{\varphi}^0 : \mathcal{A} \to \mathbb{R}^3$ and director field $\mathbf{t}^0 : \mathcal{A} \to S^2$. Material points in the reference configuration $\mathcal{B}^0 = \mathcal{S}^0 \times (c^-, c^+)$ are given by

$$\mathbf{x}^0 = \boldsymbol{\Phi}^0(\xi^1, \xi^2, \xi^3) := \boldsymbol{\varphi}^0(\xi^1, \xi^2) + \xi^3 \mathbf{t}^0(\xi^1, \xi^2), \quad \xi^3 \in (c^-, c^+) \tag{2}$$

Here and in the following, kinematic quantities in the reference configuration are distinguished from their counterparts in the current configuration by labeling them with a superscript 0.

The shell deformation is given by the composition $\boldsymbol{\chi} : \mathcal{B}^0 \to \mathcal{B}$,

$$\boldsymbol{\chi} := \boldsymbol{\Phi} \circ \left(\boldsymbol{\Phi}^0\right)^{-1} \tag{3}$$

The kinematics of the shell configurations are illustrated in Figure 1. It follows from the choice of the unit sphere as the director manifold and the invariance of h that the shell is assumed to be *rigid* in the thickness direction.

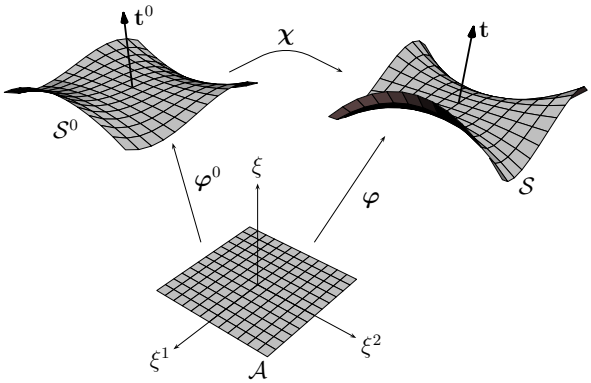

Figure 1: Reference and current configurations of the shell.

[2] In general, a collection of parameterizations will be needed to cover $\mathcal{S}$, but for simplicity they are not indexed individually here.

The covariant basis vectors in $\mathcal{S}^0$ and $\mathcal{S}$ are

$$\mathbf{a}^0_\alpha := \partial_\alpha \boldsymbol{\varphi}^0 \qquad\qquad \mathbf{a}_\alpha := \partial_\alpha \boldsymbol{\varphi}, \tag{4}$$

where the notation $\partial_\alpha := \partial/\partial\xi^\alpha$ is used to indicate partial differentiation with respect to the parametric coordinates.

The mid-surface measures in the reference and current configurations are $d\mathcal{S}^0 = \bar{j}^0 d\mathcal{A}$ and $d\mathcal{S} = \bar{j} d\mathcal{A}$, with $d\mathcal{A} := d\xi^1 d\xi^2$ and

$$\bar{j}^0 = \mathbf{t}^0 \cdot \left(\mathbf{a}^0_1 \times \mathbf{a}^0_2\right) \qquad\qquad \bar{j} = \mathbf{t} \cdot (\mathbf{a}_1 \times \mathbf{a}_2)$$

The Jacobian of the mid-surface deformation is $\bar{J} = \bar{j}/\bar{j}^0 > 0$.

The geometry of the shell is described by the surface tensors

$$a_{\alpha\beta} = \mathbf{a}_\alpha \cdot \mathbf{a}_\beta \tag{5a}$$

$$\gamma_\alpha := \mathbf{a}_\alpha \cdot \mathbf{t} \tag{5b}$$

$$\kappa_{\alpha\beta} := \mathbf{a}_\alpha \cdot \partial_\beta \mathbf{t} \tag{5c}$$

Identical definitions exist for the reference configuration. Equation (5a) gives the components of the metric tensor; (5b) measures the deviation of the director from the surface normal, that is, the relative shearing of the normal fiber; (5c) defines a curvature-like tensor. It is simple to prove that the kinematic tensors in (5) are invariant with respect to changes in frame, which is a direct consequence of the use of convected coordinates.

The components of the metric in the dual basis follow from the identity

$$a^{\alpha\beta} a_{\beta\gamma} = \delta^\alpha_\gamma$$

where the term on the right hand side is the Kronecker delta symbol. The contravariant basis vectors follow as

$$\mathbf{a}^\alpha = a^{\beta\alpha} \mathbf{a}_\beta.$$

2.2. Admissible variations

The shell is subject to the essential boundary conditions

$$\boldsymbol{\varphi} = \overline{\boldsymbol{\varphi}}, \quad \text{on } \partial_\varphi \mathcal{A} \tag{6a}$$

$$\mathbf{t} = \overline{\mathbf{t}}, \quad \text{on } \partial_t \mathcal{A} \tag{6b}$$

The shell configuration is determined uniquely by the pair $(\boldsymbol{\varphi}, \mathbf{t}) \in \boldsymbol{X} \times S^2$ through (1). In a slight abuse of notation, the pair will be written $\boldsymbol{\Phi} = (\boldsymbol{\varphi}, \mathbf{t})$. Any $\boldsymbol{\Phi}$ in the set of admissible configurations $\mathbb{X} := \boldsymbol{X} \times S^2$ is required to satisfy (6).

Admissible variations $\delta\boldsymbol{\Phi}$ of the kinematic fields are constructed by taking a curve of configurations $\varepsilon \mapsto \boldsymbol{\Phi}_\varepsilon = (\boldsymbol{\varphi}_\varepsilon, \mathbf{t}_\varepsilon)$, with $\boldsymbol{\Phi}_\varepsilon|_{\varepsilon=0} = \boldsymbol{\Phi}$, and taking $\delta\boldsymbol{\Phi} = d(\boldsymbol{\Phi}_\varepsilon)/d\varepsilon|_{\varepsilon=0}$. Thus, the set of admissible variations is

$$\mathbb{V} = \left\{\delta\boldsymbol{\Phi} = (\delta\boldsymbol{\varphi}, \delta\mathbf{t}) \colon \mathcal{A} \to \mathbb{R}^3 \times T_{\mathbf{t}} S^2 : \delta\boldsymbol{\varphi}|_{\partial_\varphi \mathcal{A}} = \mathbf{0},\ \delta\mathbf{t}|_{\partial_t \mathcal{A}} = \mathbf{0}\right\}$$

where $T_{\mathbf{t}} S^2$ is the tangent space of the unit sphere. The unit sphere is not a linear space, so the structure of the tangent space bears comment. A convenient description of $T_{\mathbf{t}} S^2$ follows from the unit length condition in S^2. Taking a curve of directors as defined above and differentiating the identity

$$\mathbf{t}_\varepsilon \cdot \mathbf{t}_\varepsilon = 1$$

gives

$$\left(\mathbf{t}_\varepsilon \cdot \frac{d}{d\varepsilon}\mathbf{t}_\varepsilon\right)\Big|_{\varepsilon=0} = 0 \tag{7}$$

which shows that members of $T_{\mathbf{t}}S^2$ are orthogonal to $\mathbf{t}$ (considering them as vectors in $\mathbb{R}^3$). That is,

$$T_{\mathbf{t}}S^2 = \left\{\mathbf{w} \in \mathbb{R}^3 : \mathbf{w} \cdot \mathbf{t} = 0\right\} \tag{8}$$

A procedure for ensuring the satisfaction of this geometric constraint in the discrete setting is discussed in Section 3.3.

2.3. Constitutive behavior

The generalized forces of the shell theory are stress resultants. Taking a set of variations $(\delta\boldsymbol{\varphi}, \delta\mathbf{t}) \in \mathbb{V}$, the conjugate pairs are

- $\mathbf{n}^\alpha$ that performs virtual work through $\partial_\alpha \delta\boldsymbol{\varphi}$,
- $\mathbf{m}^\alpha$ that performs virtual work through $\partial_\alpha \delta\mathbf{t}$,
- $\mathbf{l}$ that performs virtual work through $\delta\mathbf{t}$.

Applying the usual terminology, $\mathbf{n}^\alpha$ is the *stress resultant*, $\mathbf{m}^\alpha$ is the *stress couple resultant*, and $\mathbf{l}$ is *through-thickness stress resultant*. These can be related to the stress tensors of three dimensional continuum mechanics; see [34].

For an elastic material, there exists a free energy density function (per unit area in the reference mid-surface)

$$\psi(\partial_\alpha\boldsymbol{\varphi}, \mathbf{t}, \partial_\alpha\mathbf{t}; \partial_\alpha\boldsymbol{\varphi}^0, \mathbf{t}^0, \partial_\alpha\mathbf{t}^0).$$

The parametric dependence on $\{\partial_\alpha\boldsymbol{\varphi}^0, \mathbf{t}^0, \partial_\alpha\mathbf{t}^0\}$ highlights the fact that stretching is measured relative to the reference configuration. In the following, the explicit indication of this dependence will frequently be omitted for brevity. Using the Coleman-Noll procedure, it can be shown that the resultants are given by

$$\bar{J}\mathbf{n}^\alpha = \frac{\partial\psi(\partial_\beta\boldsymbol{\varphi}, \mathbf{t}, \partial_\beta\mathbf{t})}{\partial(\partial_\alpha\boldsymbol{\varphi})} \tag{9a}$$

$$\bar{J}\mathbf{l} = \frac{\partial\psi(\partial_\beta\boldsymbol{\varphi}, \mathbf{t}, \partial_\beta\mathbf{t})}{\partial\mathbf{t}} \tag{9b}$$

$$\bar{J}\mathbf{m}^\alpha = \frac{\partial\psi(\partial_\beta\boldsymbol{\varphi}, \mathbf{t}, \partial_\beta\mathbf{t})}{\partial(\partial_\alpha\mathbf{t})} \tag{9c}$$

The above form of the stress resultant relations is useful for writing the equilibrium equations in weak form. However, for building the constitutive framework, it is helpful to deduce the work conjugate pairs in terms of tensors intrinsic to the shell manifold. In [34] it is shown that the stress resultants can be decomposed in terms of *effective stress resultants* $\{\widetilde{n}^{\alpha\beta}, \widetilde{q}^\alpha, \widetilde{m}^{\alpha\beta}\}$ in the form

$$\mathbf{n}^\alpha = \widetilde{n}^{\alpha\beta}\partial_\beta\boldsymbol{\varphi} + \widetilde{m}^{\alpha\beta}\partial_\beta\mathbf{t} + \widetilde{q}^\alpha\mathbf{t} \tag{10a}$$

$$\mathbf{l} = \widetilde{q}^\alpha\partial_\alpha\boldsymbol{\varphi} + \underbrace{\lambda^\alpha_\mu m^{3\mu}\partial_\alpha\boldsymbol{\varphi} + l^3\mathbf{t}}_{\text{indeterminate}} \tag{10b}$$

$$\mathbf{m}^\alpha = \widetilde{m}^{\beta\alpha}\partial_\beta\boldsymbol{\varphi} + \underbrace{m^{3\alpha}\mathbf{t}}_{\text{indeterminate}} \tag{10c}$$

where λ^α_μ are components of the director in the decomposition $\partial_\mu\mathbf{t} = \lambda^\alpha_\mu\mathbf{a}_\alpha + \lambda^3_\mu\mathbf{t}$. The effective membrane resultant is required to be symmetric, $\widetilde{n}^{\alpha\beta} = \widetilde{n}^{\beta\alpha}$, by the balance of angular momentum (or equivalently,

by requiring that the internal power is invariant with respect to frame changes that are rotations). The components labeled "indeterminate" are so in the sense that they perform no work; therefore, in the weak form of the equilibrium equations they are irrelevant and may be ignored. In particular, the components of the stress couple resultant about the director, $m^{3\alpha}$—the so-called *drilling* moments—are ruled out exactly in this shell theory.

The utility of the effective stress resultants is that they are work conjugate to the variations of the kinematic surface tensors in (5). The free energy density function may be further specified to depend on the kinematics solely though the surface tensors, as in

$$\psi(\partial_\alpha \boldsymbol{\varphi}, \mathbf{t}, \partial_\alpha \mathbf{t}; \partial_\alpha \boldsymbol{\varphi}^0, \mathbf{t}^0, \partial_\alpha \mathbf{t}^0) = \widehat{\psi}(a_{\alpha\beta}, \gamma_\alpha, \kappa_{\alpha\beta}; a^0_{\alpha\beta}, \gamma^0_\alpha, \kappa^0_{\alpha\beta}).$$

The stress relations then follow from the Coleman-Noll procedure as

$$\bar{J}\widetilde{n}^{\alpha\beta} = 2\frac{\partial \widehat{\psi}(a_{\alpha\beta}, \gamma_\alpha, \kappa_{\alpha\beta})}{\partial a_{\alpha\beta}} \tag{11a}$$

$$\bar{J}\widetilde{m}^{\alpha\beta} = \frac{\partial \widehat{\psi}(a_{\alpha\beta}, \gamma_\alpha, \kappa_{\alpha\beta})}{\partial \kappa_{\alpha\beta}} \tag{11b}$$

$$\bar{J}\widetilde{q}^{\alpha} = \frac{\partial \widehat{\psi}(a_{\alpha\beta}, \gamma_\alpha, \kappa_{\alpha\beta})}{\partial \gamma_\alpha}. \tag{11c}$$

The effective stress resultants and the kinematic tensors are invariant with respect to changes in frame, thus specifying the constitutive equations in this form guarantees frame indifference.

2.4. Equilibrium equations

Equilibrium positions of the shell are stationary points of the potential energy functional

$$J(\boldsymbol{\Phi}) = \int_{\mathcal{S}^0} \psi(\partial_\alpha \boldsymbol{\varphi}, \mathbf{t}, \partial_\alpha \mathbf{t})\, d\mathcal{S}^0 - \mathcal{W}_{\text{ext}}(\boldsymbol{\Phi}) \tag{12}$$

The linear functional of the external work comprises body and boundary contributions:

$$\mathcal{W}_{\text{ext}}(\boldsymbol{\Phi}) = \int_{\mathcal{S}} (\mathbf{f} \cdot \boldsymbol{\varphi} + \boldsymbol{\tau} \cdot \mathbf{t})\; d\mathcal{S} + \int_{\partial_N \mathcal{A}} \bar{\mathbf{n}} \cdot \boldsymbol{\varphi}\, \bar{j} ds + \int_{\partial_M \mathcal{A}} \bar{\mathbf{m}} \cdot \mathbf{t}\, \bar{j} ds. \tag{13}$$

The source term $\mathbf{f}^0$ is an equivalent distributed force (per unit area in the current configuration) acting on the mid-surface, which encapsulates volumetric body forces on the shell, as well as tractions on the top and bottom surfaces. Similarly, $\boldsymbol{\tau}$ is a distributed couple. The generalized forces $\bar{\mathbf{n}}$ and $\bar{\mathbf{m}}$ are prescribed resultant tractions. To ensure well-posed problems, the regions of the essential and natural boundary conditions are taken to satisfy

$$\partial_{\boldsymbol{\varphi}}\mathcal{A} \cap \partial_N \mathcal{A} = \varnothing, \quad \partial_{\boldsymbol{\varphi}} A \cup \partial_N \mathcal{A} = \partial\mathcal{A}$$

and

$$\partial_{\mathbf{t}}\mathcal{A} \cap \partial_M \mathcal{A} = \varnothing, \quad \partial_{\mathbf{t}}\mathcal{A} \cup \partial_M \mathcal{A} = \partial\mathcal{A}$$

Futhermore, $\partial_{\boldsymbol{\varphi}}\mathcal{A}$ is assumed to have positive Lebesgue measure to rule out rigid body motions.

Equilibrium positions are found by the vanishing of the first variation of the energy

$$0 = \langle DJ(\boldsymbol{\Phi}), \delta\boldsymbol{\Phi} \rangle = \frac{d}{d\varepsilon}\bigg|_{\varepsilon=0} J(\boldsymbol{\Phi}_\varepsilon) \tag{14}$$

for all admissible variations $\delta\mathbf{\Phi} = (\delta\boldsymbol{\varphi}, \delta\mathbf{t})$. *Stable* equilibrium positions constitute local minimizers of (12). The variation of the energy functional is given explicitly by

$$\langle DJ(\mathbf{\Phi}), \delta\mathbf{\Phi}\rangle = \underbrace{\int_{\mathcal{S}^0} \left(\mathbf{n}^\alpha \cdot \partial_\alpha \delta\boldsymbol{\varphi} + \mathbf{m}^\alpha \cdot \partial_\alpha \delta\mathbf{t} + \mathbf{l}\cdot\delta\mathbf{t}\right)\, \bar{J} d\mathcal{S}^0}_{\mathcal{W}_{\text{int}}(\mathbf{\Phi};\delta\mathbf{\Phi})} - \mathcal{W}_{\text{ext}}(\delta\mathbf{\Phi}) \tag{15}$$

Equation (15) is the virtual work equation of the shell.

For the purposes of finite element discretization, the weak form of the equilibrium equations (14) is the only object required. However, for completeness, the equilibrium equations in strong form are recorded here. Assuming sufficient smoothness, the divergence theorem applied to the virtual work yields

$$\int_{\mathcal{A}} \left\{ \left[-\partial_\alpha\left(\bar{j}\mathbf{n}^\alpha\right) - \bar{j}\mathbf{f}\right]\cdot\delta\boldsymbol{\varphi} + \left[-\partial_\alpha(\bar{j}\mathbf{m}^\alpha) + \bar{j}\mathbf{l} - \bar{j}\boldsymbol{\tau}\right]\cdot\delta\mathbf{t}\right\} d\xi^1 d\xi^2 \\ + \int_{\partial_N\mathcal{A}} (\mathbf{n}^\alpha\nu_\alpha - \bar{\bar{\mathbf{n}}})\cdot\delta\boldsymbol{\varphi}\,\bar{j}ds + \int_{\partial_M\mathcal{A}} (\mathbf{m}^\alpha\nu_\alpha - \bar{\bar{\mathbf{m}}})\cdot\delta\mathbf{t}\,\bar{j}ds = 0, \quad \forall(\delta\boldsymbol{\varphi},\delta\mathbf{t})\in\mathbb{V}$$

where $\boldsymbol{\nu}$ is the (in-plane) outward unit normal vector to $\partial\mathcal{S}$, with components $\nu_\alpha = \boldsymbol{\nu}\cdot\mathbf{a}_\alpha$. The Euler-Lagrange equations are thus

$$\left.\begin{aligned}\partial_\alpha(\bar{j}\mathbf{n}^\alpha) + \bar{j}\mathbf{f} &= \mathbf{0}\\ \partial_\alpha(\bar{j}\mathbf{m}) - \bar{j}\mathbf{l} + \bar{j}\boldsymbol{\tau} &= \mathbf{0}\end{aligned}\right\} \text{ in } \mathcal{A} \tag{16}$$

$$\begin{aligned}\mathbf{n}^\alpha\nu_\alpha &= \bar{\bar{\mathbf{n}}} \quad \text{on } \partial_N\mathcal{A}\\ \mathbf{m}^\alpha\nu_\alpha &= \bar{\bar{\mathbf{m}}} \quad \text{on } \partial_M\mathcal{A}\end{aligned} \tag{17}$$

which are supplemented by the essential boundary conditions. The first of (16) is the balance of linear momentum, and the second is the balance of angular momentum.

2.5. Specification of the constitutive equations

In this paper, all examples are shown with a simple isotropic hyperelasticity model. Membrane, shear, and bending strains are defined as

$$\epsilon_{\alpha\beta} = \frac{1}{2}\left(a_{\alpha\beta} - a^0_{\alpha\beta}\right) \qquad \zeta_\alpha = \gamma_\alpha - \gamma^0_\alpha \qquad \rho_{\alpha\beta} = \kappa_{\alpha\beta} - \kappa^0_{\alpha\beta} \tag{18}$$

respectively. The free energy is taken as $\psi = \overline{\psi}(\epsilon_{\alpha\beta}, \zeta_\alpha, \rho_{\alpha\beta})$, where

$$\overline{\psi}(\epsilon_{\alpha\beta},\zeta_\alpha,\rho_{\alpha\beta}) = \frac{1}{2}\left(t\epsilon_{\alpha\beta}H^{\alpha\beta\gamma\delta}\epsilon_{\gamma\delta} + tk\mu\zeta_\alpha a^{0^{\alpha\beta}}\zeta_\beta + \frac{t^3}{12}\rho_{\alpha\beta}H^{\alpha\beta\gamma\delta}\rho_{\gamma\delta}\right)$$

In the above, t is the shell thickness, μ is the shear modulus, k is the shear reduction coefficient (taken as 5/6), and $H^{\alpha\beta\gamma\delta}$ is the plane stress elastic tensor

$$H^{\alpha\beta\gamma\delta} = \frac{\mu}{2}(a^{0^{\alpha\gamma}}a^{0^{\beta\delta}} + a^{0^{\alpha\delta}}a^{0^{\beta\gamma}}) + \frac{E\nu}{1-\nu^2}a^{0^{\alpha\beta}}a^{0^{\gamma\delta}}.$$

The elastic modulus E, the Poisson's ratio ν, and the shear modulus μ are of course related through $\mu = E/[2(1+\nu)]$.

According to (11), the effective stress resultants are

$$\bar{J}\widetilde{n}^{\alpha\beta} = tH^{\alpha\beta\gamma\delta}\epsilon_{\gamma\delta} \qquad \bar{J}\widetilde{q}^{\alpha} = tk\mu a^{0\,\alpha\beta}\zeta_{\beta} \qquad \bar{J}\widetilde{m}^{\alpha\beta} = \frac{t^3}{12}H^{\alpha\beta\gamma\delta}\rho_{\gamma\delta} \tag{19}$$

3. Discontinuous Galerkin discretization

In the following, function spaces of vector fields are indicated with bold typeface, e.g., $\boldsymbol{X}$. Vector-valued spaces are composed of Cartesian products of scalar spaces, which are indicated with the same letter with italic typeface, e.g., $\boldsymbol{X} = [X]^3$. Let $\mathcal{T}_h$ be a conforming collection of isoparametric triangle elements interpolating the shell mid-surface, $\mathcal{S} \simeq \mathcal{S}_h = \cup_{E\in\mathcal{T}_h} E$. The set of all edges in the triangulation is written $\Gamma = \cup_{E\in\mathcal{T}_h}\partial E$. The symbol Γ_I signifies the set of all internal edges, $\Gamma_I = \Gamma \setminus \partial\mathcal{S}$.

3.1. Mid-surface position interpolation

Each $E \in \mathcal{T}_h$ is the image of a master element $\hat{E} \subseteq \mathbb{R}^2$ under the position map $E = \boldsymbol{\varphi}_h(\hat{E}) \in \boldsymbol{X}_h$. The discontinuous Galerkin function space for the positions $\boldsymbol{X}_h$ is built up from a collection of smooth discrete function spaces $\boldsymbol{X}_h^E \subseteq \boldsymbol{H}^1(\hat{E})$ as

$$\boldsymbol{X}_h = \prod_{E\in\mathcal{T}_h} \boldsymbol{X}_h^E$$

The element-wise spaces are taken to be $\boldsymbol{X}_h^E = [\mathcal{P}_k(\hat{E})]^3$, $k \geq 2$, where $\mathcal{P}_k(\hat{E})$ is the set of polynomial of degree at most k on the master element. Note that with this definition, the position vector can have jumps on Γ_I. In this work, boundary conditions are enforced strongly; consequently, functions in $\boldsymbol{X}_h$ are required to satisfy the essential boundary conditions on $\partial_\varphi\mathcal{A}$.

A standard Lagrange polynomial basis is taken. Writing N^A for the basis functions, the interpolation of the mid-surface position is written

$$\boldsymbol{\varphi}(\xi^1,\xi^2) = \sum_{A=1}^{n_x} N^A(\xi^1,\xi^2)\bar{\mathbf{x}}_A \tag{20}$$

where $n_x = (k+1)(k+2)/2$ is the number of position nodes per element. The symbol N_x will be used to denote the number of position nodes in all $\mathcal{T}_h$. Because discontinuous Galerkin basis functions have support only over a single element, it is natural to identify the global basis functions with the corresponding elemental basis functions, and the same symbol N^A is used for both subsequently. The reference mid-surface map $\boldsymbol{\varphi}_h^0 \in \boldsymbol{X}_h$ is constructed identically.

Following the Galerkin prescription, variations of the position $\delta\boldsymbol{\varphi}$ are given by

$$\delta\boldsymbol{\varphi}(\xi^1,\xi^2) = \sum_{A=1}^{n_x} N^A(\xi^1,\xi^2)\delta\bar{\mathbf{x}}_A.$$

The set of discrete variations is written $\mathbf{V}_h$. Due to the adopted strong enforcement of boundary conditions, functions in $\mathbf{V}_h$ are required to vanish on $\partial_\varphi\mathcal{A}$.

3.2. Interpolation of the director

Writing $\boldsymbol{T}_h$ for the space of the directors, a discontinuous Galerkin space is constructed from element-wise spaces $\boldsymbol{T}_h^E \subseteq \boldsymbol{H}^1(\hat{E})$, according to

$$\boldsymbol{T}_h = \prod_{E\in\mathcal{T}_h} \boldsymbol{T}_h^E, \quad \boldsymbol{T}_h^E = [\mathcal{P}_{k-1}(\hat{E})]^3$$

The function spaces of the discrete kinematic fields thus satisfies the natural compatibility condition $D\boldsymbol{X}_h \subseteq \boldsymbol{T}_h$. This is a key step to preventing locking.

A Lagrange polynomial basis is also taken for the representation of the discrete director field $\mathbf{t}_h$. The interpolation is written

$$\mathbf{t}_h(\xi^1,\xi^2) = \sum_{A}^{n_T} L^A(\xi^1,\xi^2)\mathbf{t}_A \tag{21}$$

where $\mathbf{t}_A \in S^2$ are nodal director values and $n_T = k(k+1)/2$ is the number of director nodes per element. In the following, N_T will signify the number of director nodes in the entire mesh. At points inside an element, the linear interpolation does not guarantee $\|\mathbf{t}_h\| = 1$ (and thus $\mathbf{t}_h \notin S^2$), but the deviation is bounded by the interpolation error. A kinematic update procedure is adopted (described in Section 3.8) that strictly observes the unit length constraint of the nodal directors as the shell deforms.

The nodal values of the director field in the reference configuration is taken as

$$\mathbf{t}_A^0 = \frac{\partial_1\boldsymbol{\varphi}_h^0 \times \partial_2\boldsymbol{\varphi}_h^0}{\|\partial_1\boldsymbol{\varphi}_h^0 \times \partial_2\boldsymbol{\varphi}_h^0\|}.$$

which is the surface normal vector (i.e., the out-of-plane normal). However, the piecewise polynomial representation of the reference mid-surface $\mathcal{S}_h^0$ is only C^0 in general, and the surface normal vector suffers jumps across element edges. When treating smooth shells, it is inconvenient to have jumps in the reference configuration, as these jumps would need to be stored and subtracted out of the DG derivatives to avoid inducing spurious strain energy in the reference configuration. To circumvent this problem, a unique value is assigned to all spatially coincident director nodes on element boundaries by arbitrarily selecting one of the nodal values. It bears emphasis that the orientation of the reference director field does not affect the response of the shell, but rather only the deviation from it during the deformation. In our numerical implementation, the nodal values from the element with the smallest global index are chosen for this purpose.

Non-manifold cases, such as finite kinks and T-junctions, can be detected and handled during this pre-processing step; see, e.g., [35]. Such complications are not treated presently.

3.3. Interpolation of director variations

To preserve the essential geometric structure of S^2 when constructing director variations in the discrete shell, the parameterization of the unit sphere advocated by Simo, Fox, and Rifai in [36] is adopted. Recall that director variations are members of $T_{\mathbf{t}}S^2$ (cf. (7)), which may be considered as vectors in the plane tangent to S^2 at $\mathbf{t}$; see Figure 2. A rotation tensor $\boldsymbol{\Lambda} \in SO(3)$ is constructed with the property

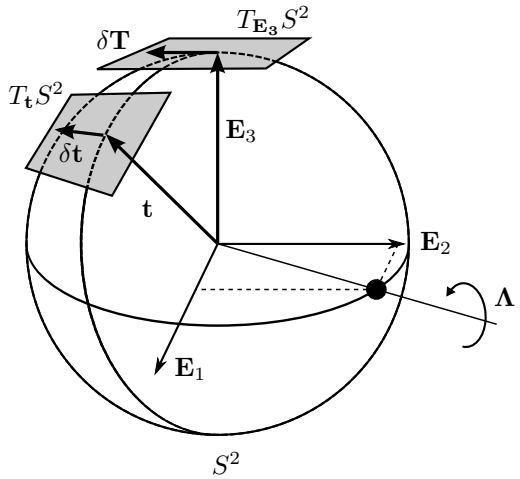

Figure 2: Parameterization of the unit sphere and its tangent space. The director $\mathbf{t}$ is the image of $\mathbf{E}_3$ under the rotation $\boldsymbol{\Lambda}$.

$$\mathbf{t} = \mathbf{\Lambda}\mathbf{E}_3 \tag{22}$$

and where the rotation axis is *orthogonal* to $\mathbf{E}_3$. This rotation tensor is unique, and in fact has an explicit representation using Rodrigues' formula:

$$\mathbf{\Lambda} = (\mathbf{t}\cdot\mathbf{E}_3)\mathbf{1} + (\widehat{\mathbf{E}_3\times\mathbf{t}}) + \frac{1}{1+\mathbf{t}\cdot\mathbf{E}_3}(\mathbf{E}_3\times\mathbf{t})\otimes(\mathbf{E}_3\times\mathbf{t}) \tag{23}$$

The operation $\widehat{\bullet}:\mathbb{R}^3\to so(3)$ indicates the skew cross product tensor associated to a vector.[3] The utility of this rotation is that it allows a simple representation of $\delta\mathbf{t}\in T_{\mathbf{t}}S^2$ with only 2 degrees of freedom. Referring again to Figure 2, $\mathbf{\Lambda}$ takes vectors in $T_{\mathbf{E}_3}S^2$ to $T_{\mathbf{t}}S^2$ along a great circle (i.e., a geodesic of S^2). The space $T_{\mathbf{E}_3}S^2$ is a plane perpendicular to $\mathbf{E}_3$, and thus is isomorphic to $\mathbb{R}^2$. Taking advantage of this isomorphism, any $\delta\mathbf{T}\in T_{\mathbf{E}_3}S^2$ can be represented as

$$\delta\mathbf{T} = \delta T^1\mathbf{E}_1 + \delta T^2\mathbf{E}_2.$$

Then $\delta\mathbf{t}\in T_{\mathbf{t}}S^2$ can be defined

$$\delta\mathbf{t} = \bar{\mathbf{\Lambda}}\delta\mathbf{T} \tag{24}$$

where $\bar{\mathbf{\Lambda}}:\mathbb{R}^2\to\mathbb{R}^3$ is the tensor formed from the first two columns of the matrix of $\mathbf{\Lambda}$; that is,

$$\bar{\mathbf{\Lambda}} = \Lambda^i_\alpha\mathbf{E}_i\otimes\mathbf{E}^\alpha \tag{25}$$

The 2 degree of freedom vector $\delta\mathbf{T}$ is referred to as the *material* director variation, and $\delta\mathbf{t}$ is called the *spatial* director variation. This parameterization automatically guarantees $\mathbf{t}\cdot\delta\mathbf{t}=0$.

Discrete versions of the director variations and other members of $T_{\mathbf{t}}S^2$ are constructed as follows. Equation (24) is employed to construct *nodal* values of the director variation, viz.

$$\delta\mathbf{t}_A = \bar{\mathbf{\Lambda}}_A\delta\mathbf{T}_A,\quad \delta\mathbf{T}_A\in\mathbb{R}^2,\ A=1,\ldots,N_T \tag{26}$$

The nodal rotation tensors $\mathbf{\Lambda}_A$ are computed from the Rodrigues formula above and stored for every node of the director interpolation at the start of the simulation. A geometrically exact procedure for updating $\mathbf{\Lambda}_A$ as the shell deforms is given in Section 3.8.

Variations of the discrete director field $\delta\mathbf{t}$ are interpolated with the same basis as the directors, i.e.,

$$\delta\mathbf{t} = \sum_A^{n_t} L^A\delta\mathbf{t}_A = \sum_A^{n_t} L^A\bar{\mathbf{\Lambda}}_A\delta\mathbf{T}_A \tag{27}$$

The set of discrete director variations is denoted by $T_{\mathbf{t}_h}\boldsymbol{T}_h$. The kinematic boundary conditions on the director field are enforced strongly; members of $T_{\mathbf{t}_h}\boldsymbol{T}_h$ are thus required to vanish on $\partial_t\mathcal{A}$.

The linearized corrections returned by iterative procedures, such as Newton's method, are also admissible variations, and are interpolated as elements of $T_{\mathbf{t}_h}\boldsymbol{T}_h$ in the discrete setting as well. This implies that the director field has two degrees of freedom at each node. The parameterization described above eliminates drilling degrees of freedom identically. This is at variance with many other shell discretizations that rely on additional assumptions and ad hoc numerical techniques to control drilling degrees of freedom.

[3] That is, for an arbitrary $\mathbf{a}\in\mathbb{R}^3$, $\widehat{\mathbf{a}}$ is the tensor with the matrix representation in the canonical basis

$$[\widehat{\mathbf{a}}] = \begin{bmatrix} 0 & -a^3 & a^2 \\ a^3 & 0 & -a^1 \\ -a^2 & a^1 & 0 \end{bmatrix}$$

In order to write subsequent equations more compactly, the notation

$$\mathbb{X}_h := \boldsymbol{X}_h \times \boldsymbol{T}_h \qquad \text{the trial solution space}$$
$$\mathbb{V}_h := \boldsymbol{V}_h \times T_{\mathbf{t}_h}\boldsymbol{T}_h \qquad \text{the variation space}$$

is introduced.

3.4. Discontinuous Galerkin derivative operator

A common feature of discontinuous Galerkin methods is the projection of the gradient onto a discrete function space. Following the primal formulation of DG methods in [37], the projection will be used to define a discrete derivative operator. (Applying the terminology in [20], this operator will be called the *DG derivative*). The DG derivative formulated here operates with respect to the *convected coordinates* instead of the more common fixed Cartesian frame. An explicit derivation is given for the DG derivatives of the discrete mid-surface position space $\boldsymbol{X}_h$; the definition for the DG derivative operator over the discrete director space $\boldsymbol{T}_h$ is analogous and will be omitted to avoid being repetitious. At the close of the section, the final result of the DG derivative operator of the director is given to fix the notation.

To begin, a DG piecewise polynomial function space, denoted by W_h, composed as the Cartesian product of elemental spaces $W_h^E \subseteq H^1(\hat{E})$, is chosen to approximate the derivatives of the position components with respect to the convected coordinates. This space is required to satisfy $DX_h \subseteq W_h$. Taking an arbitrary smooth function u, the derivative

$$w_\alpha = \partial_\alpha u$$

can be written in a weak form by formally multiplying by a test function $z^\alpha \in W_h$, integrating over $\hat{E}$, the image of element $E \in \mathcal{T}_h$ under the coordinate chart (i.e., the master element), and integrating by parts:

$$\int_{\hat{E}} w_\alpha z^\alpha \, d\mathcal{A} = -\int_{\hat{E}} u \, \partial_\alpha z^\alpha \, d\mathcal{A} + \int_{\partial\hat{E}} u z^\alpha \mu_\alpha^{\hat{E}} \, ds$$

The vector $\boldsymbol{\mu}^{\hat{E}} = \mu_\alpha^{\hat{E}} \mathbf{E}^\alpha$ is the outward unit normal to $\partial\hat{E}$. This identity, satisfied by any $u \in H^1(\hat{E})$, serves as the motivation for the definition of the DG derivative. A function $(w_h)_\alpha \in W_h$ approximating the derivatives of $u_h \in X_h$ is sought by defining

$$\int_{\hat{E}} (w_h)_\alpha z^\alpha \, d\mathcal{A} = -\int_{\hat{E}} u_h \partial_\alpha z^\alpha \, d\mathcal{A} + \int_{\partial\hat{E}} \widehat{u}(u_h) z^\alpha \mu_\alpha^{\hat{E}} \, ds, \quad \forall z^\alpha \in W_h \tag{28}$$

where $\widehat{u}\colon X_h \to T(\Gamma)$ is a *numerical trace*, to be specified as part of the method, that approximates u on $\partial\hat{E}$. Summing (28) over all the elements yields

$$\int_{\hat{E}} (w_h)_\alpha z^\alpha \, d\mathcal{A} = -\int_{\hat{E}} u_h \partial_{h\alpha} z^\alpha \, d\mathcal{A} + \sum_{E\in\mathcal{T}_h} \int_{\partial\hat{E}} \widehat{u}(u_h) z^\alpha \mu_\alpha^{\hat{E}} ds, \quad \forall z^\alpha \in W_h \tag{29}$$

Here and in the following, a subscript h is attached to the differential operator to indicate that it is to be applied in the piecewise sense, element by element in $\mathcal{T}_h$.

To proceed, some trace operators are defined. For each edge $e \in \Gamma_I$, the two elements sharing the edge are designated arbitrarily as E^+ and E^-. The jump $[\![\bullet]\!]$ and average $\{\bullet\}$ operators are defined

$$[\![\bullet]\!] = \bullet^- - \bullet^+ \qquad\qquad \{\bullet\} = \frac{1}{2}\left(\bullet^+ + \bullet^-\right) \tag{30}$$

where the superscript identifies which side of the edge the restriction of the field is taken, e.g., $u^- = u|_{\partial E^-}$.

A simple algebraic manipulation shows that

$$\sum_{E\in\mathcal{T}_h} \int_{\partial\hat{E}} a b^\alpha \mu_\alpha^E \, ds = \int_{\Gamma_I} \left([\![a]\!] \{b^\alpha\} \mu_\alpha + \{a\} [\![b^\alpha]\!] \mu_\alpha \right) ds + \int_{\partial\mathcal{A}} a b^\alpha \mu_\alpha \, ds \tag{31}$$

Applying (31) to (29) gives

$$\int_{\mathcal{A}} (w_h)_\alpha z^\alpha \, d\mathcal{A} = -\int_{\mathcal{A}} u_h \partial_{h\alpha} z^\alpha \, d\mathcal{A} + \int_{\Gamma_I} \left([\![\widehat{u}]\!] \{z^\alpha\} \mu_\alpha + \{\widehat{u}\} [\![z^\alpha]\!] \mu_\alpha \right) ds + \int_{\partial\mathcal{A}} \widehat{u} z^\alpha \mu_\alpha \, ds, \quad \forall z^\alpha \in W_h \tag{32}$$

Integrating the first term on the right hand side by parts, element by element, and again using (31) yields

$$\int_{\mathcal{A}} (w_h)_\alpha z^\alpha \, d\mathcal{A} = \int_{\mathcal{A}} \partial_{h\alpha} u_h z^\alpha \, d\mathcal{A} + \int_{\Gamma_I} \left([\![\widehat{u} - u_h]\!] \{z^\alpha\} \mu_\alpha \right. \tag{33}$$

$$\left. + \{\widehat{u} - u_h\} [\![z^\alpha]\!] \mu_\alpha \right) ds + \int_{\partial\mathcal{A}} (\widehat{u} - u_h) z^\alpha \mu_\alpha \, ds \tag{34}$$

To obtain an explicit formula for $(w_h)_\alpha$, we introduce lifting operators on the interior edges $r_\alpha \colon L^2(\Gamma_I) \to W_h$, $l_\alpha \colon L^2(\Gamma^I) \to W_h$, and a boundary lifting operator $r_\alpha^\partial \colon L^2(\partial\mathcal{S}) \to W_h$. These are linear operators defined by the identities

$$\int_{\mathcal{A}} r_\alpha(a) b^\alpha \, d\mathcal{A} = -\int_{\Gamma_I} a \{b^\alpha\} \mu_\alpha \, ds, \quad \forall b^\alpha \in W^h \tag{35}$$

$$\int_{\mathcal{A}} l_\alpha(a) b^\alpha \, d\mathcal{A} = -\int_{\Gamma_I} a [\![b^\alpha]\!] \mu_\alpha \, ds, \quad \forall b^\alpha \in W^h \tag{36}$$

$$\int_{\mathcal{A}} r_\alpha^\partial(a) b^\alpha \, d\mathcal{A} = -\int_{\partial\mathcal{A}} a b^\alpha \mu_\alpha \, ds, \quad \forall b^\alpha \in W^h \tag{37}$$

Applying these definitions to (33) gives

$$\int_{\mathcal{A}} \left[(w_h)_\alpha - \partial_{h\alpha} u_h + r_\alpha \left([\![\widehat{u} - u_h]\!] \right) + l_\alpha \left(\{\widehat{u} - u_h\} \right) + r_\alpha^\partial \left(\widehat{u} - u_h \right) \right] z^\alpha \, d\mathcal{A} = 0, \quad \forall z^\alpha \in W_h \tag{38}$$

Recalling that $DX_h \subset W_h$, and that the lifting operators themselves reside in W_h, the above holds only if

$$(w_h)_\alpha = \partial_\alpha^{\mathrm{DG}} u_h = \partial_{h\alpha} u_h - r_\alpha \left([\![\widehat{u} - u_h]\!] \right) - l_\alpha \left(\{\widehat{u} - u_h\} \right) - r_\alpha^\partial \left(\widehat{u} - u_h \right) \tag{39}$$

which yields the sought projection of the derivative of u_h onto the space W_h, in the sense of (28).

The DG derivative on scalar fields defined above is extended to vector fields in the standard way, component by component. Specifically, the DG derivative of $\mathbf{X}_h \ni \boldsymbol{\varphi} = \varphi_i \mathbf{E}^i$ is $\partial_\alpha^{\mathrm{DG}} \boldsymbol{\varphi} := (\partial_\alpha^{\mathrm{DG}} \varphi_i) \mathbf{E}^i$. This leads to trivial vector extensions of the lifting operator, such as $\mathbf{r}_\alpha(\boldsymbol{\varphi}) = r_\alpha(\varphi_i) \mathbf{E}^i$. With the vector field DG derivative thus defined, the DG derivative of the position map is then

$$\partial_\alpha^{\mathrm{DG}} \boldsymbol{\varphi}_h = \partial_{h\alpha} \boldsymbol{\varphi}_h - \mathbf{r}_\alpha \left([\![\widehat{\boldsymbol{\varphi}} - \boldsymbol{\varphi}_h]\!] \right) - \mathbf{l}_\alpha \left(\{\widehat{\boldsymbol{\varphi}} - \boldsymbol{\varphi}_h\} \right) - \mathbf{r}_\alpha^\partial \left(\widehat{\boldsymbol{\varphi}} - \boldsymbol{\varphi}_h \right) \tag{40}$$

Applying the same formulation in this section to the director field yields a DG derivative over the discrete director space $\boldsymbol{T}_h$. By a slight abuse of notation, the same symbol $\partial_\alpha^{\mathrm{DG}}$ is used for the DG derivative of the director field, although the underlying function spaces are different. The approximation space for the director derivative (i.e., the director counterpart to W_h) is denoted K_h. The corresponding lifting operators for the director field are written in a sans serif font: $\mathsf{r}_\alpha, \mathsf{l}_\alpha, \mathsf{r}_\alpha^\partial \in K_h$. The DG derivative of the director is $\partial_\alpha^{\mathrm{DG}} \colon \mathbf{T}_h \to \mathbf{K}_h$,

$$\partial_\alpha^{\mathrm{DG}} \mathbf{t}_h = \partial_{h\alpha} \mathbf{t}_h - \mathbf{r}_\alpha \left(\left[\!\!\left[\widehat{\mathbf{t}} - \mathbf{t}_h \right]\!\!\right] \right) - \mathbf{l}_\alpha \left(\left\{ \widehat{\mathbf{t}} - \mathbf{t}_h \right\} \right) - \mathbf{r}_\alpha^\partial \left(\widehat{\mathbf{t}} - \mathbf{t}_h \right) \tag{41}$$

where the boldface type on the lifting operators indicates the same extension to vector fields, e.g., $\mathbf{r}_\alpha(\mathbf{t}) = \mathsf{r}_\alpha(t_i) \mathbf{E}^i$.

The polynomial spaces of the DG derivative spaces W_h and K_h are chosen as follows. Extending the strategy advocated by Arnold et al. [24], the polynomial space W_h^E for the DG derivatives of the position field is taken to be the same as the director space T_h^E, specifically, $W_h^E = \mathcal{P}_{k-1}(E)$. With this choice, $\partial_\alpha^{\mathrm{DG}} \boldsymbol{\varphi} \in \boldsymbol{T}_h$ for every $\boldsymbol{\varphi} \in \boldsymbol{X}_h$. This is essential to satisfy the thin shell compatibility condition and therefore to prevent locking. The elemental director derivative space K_h^E is not limited by locking concerns, but for simplicity is also taken to be $K_h^E = \mathcal{P}_{k-1}(E)$.

3.5. Specification of the numerical traces

The definition of the DG derivative is completed by choosing a numerical trace operator. The choice of numerical trace affects the numerical properties of the method, including consistency, accuracy, and the bandwidth of the stiffness matrix; a discussion of these issues is presented in [37]. In this work, simple average traces are employed:

$$\widehat{\boldsymbol{\varphi}}(\boldsymbol{\psi}) = \begin{cases} \{\boldsymbol{\psi}\} & \text{on } \Gamma_I \\ \overline{\boldsymbol{\varphi}} \text{ or } \mathbf{0} & \text{on } \partial_{\boldsymbol{\varphi}}\mathcal{A} \\ \boldsymbol{\psi} & \text{on } \partial_n \mathcal{A} \end{cases} \qquad \widehat{\mathbf{t}}(\mathbf{s}) = \begin{cases} \{\mathbf{s}\} & \text{on } \Gamma_I \\ \overline{\mathbf{t}} \text{ or } \mathbf{0} & \text{on } \partial_{\mathbf{t}}\mathcal{A} \\ \mathbf{s} & \text{on } \partial_m \mathcal{A} \end{cases} \tag{42}$$

The kinematic boundary conditions are enforced strongly, hence the boundary trace is taken to be the prescribed value on the essential boundary to eliminate the boundary lifting operator. That is, on $\partial_\varphi \mathcal{A}$, the numerical trace of the displacement is $\widehat{\boldsymbol{\varphi}}(\boldsymbol{\varphi}_h) = \overline{\boldsymbol{\varphi}}$ and the numerical trace of the virtual displacement is $\widehat{\boldsymbol{\varphi}}(\delta\boldsymbol{\varphi}) = \mathbf{0}$. With these choices the DG derivatives become

$$\partial_\alpha^{\mathrm{DG}} \boldsymbol{\varphi}_h = \partial_{h\alpha} \boldsymbol{\varphi}_h + \mathbf{r}_\alpha([\![\boldsymbol{\varphi}_h]\!]) \tag{43}$$

$$\partial_\alpha^{\mathrm{DG}} \mathbf{t}_h = \partial_{h\alpha} \mathbf{t}_h + \mathbf{r}_\alpha([\![\mathbf{t}_h]\!]) \tag{44}$$

3.6. Discrete form of the equilibrium equations

The discontinuous Galerkin method is derived from a discrete energy functional $J_h \colon \mathbb{X}_h \to \mathbb{R}$. As in [20], the discrete energy functional is consistently formulated by formally replacing the derivative operator in the continuous potential energy with the DG derivative operator. To this functional, standard DG stabilization terms are also added, yielding

$$\begin{aligned} J_h(\boldsymbol{\Phi}_h) = &\int_{\mathcal{S}_h^0} \psi(\partial_\alpha^{DG} \boldsymbol{\varphi}_h, \mathbf{t}_h, \partial_\alpha^{DG} \mathbf{t}_h)\, d\mathcal{S}^0 - \mathcal{W}_{\mathrm{ext}}(\boldsymbol{\varphi}_h, \mathbf{t}_h) \\ &+ \frac{1}{2}\mathcal{W}_{\mathrm{x,stab}}(\boldsymbol{\varphi}_h, \boldsymbol{\varphi}_h) + \frac{1}{2}\mathcal{W}_{\mathrm{T,stab}}(\mathbf{t}_h, \mathbf{t}_h). \end{aligned} \tag{45}$$

The stabilization terms are given by

$$\mathcal{W}_{\mathrm{x,stab}}(\boldsymbol{\eta}, \boldsymbol{\omega}) := \int_{\Gamma_I} \frac{\beta_x}{h^e} [\![\boldsymbol{\eta}]\!] \cdot [\![\boldsymbol{\omega}]\!]\, \bar{j}^0 ds, \quad \boldsymbol{\eta}, \boldsymbol{\omega} \in \boldsymbol{X}_h \tag{46}$$

$$\mathcal{W}_{\mathrm{T,stab}}(\mathbf{v}, \mathbf{w}) := \int_{\Gamma_I} \frac{\beta_T}{h^e} [\![\mathbf{v}]\!] \cdot [\![\mathbf{w}]\!]\, \bar{j}^0 ds, \quad \mathbf{v}, \mathbf{w} \in \boldsymbol{T}_h \tag{47}$$

The symbol h^e is a local measure of the mesh diameter, here taken as the length of the edge. For the present work, the penalty parameters are normalized by taking $\beta_x = c_x E t$ and $\beta_T = c_T E t^3/12$, where t is the shell thickness, E is the Young's modulus of the material, and c_x, c_T are positive real numbers taken sufficiently large.

Equilibrium configurations of the discrete shell are given by the stationary points of (45). The equilibrium

equations thus follow as

$$\begin{aligned}\langle DJ_h(\boldsymbol{\Phi}_h), \delta\boldsymbol{\Phi}\rangle = 0 = \int_{\mathcal{S}_h^0} \left(\mathbf{n}^\alpha \cdot \partial_\alpha^{\mathrm{DG}}\delta\boldsymbol{\varphi} + \mathbf{l}\cdot\delta\mathbf{t} + \mathbf{m}^\alpha \cdot \partial_\alpha^{\mathrm{DG}}\delta\mathbf{t}\right)\, \bar{J}d\mathcal{S}^0 \\ - \mathcal{W}_{\mathrm{ext}}(\delta\boldsymbol{\Phi}) + \mathcal{W}_{\mathrm{x,stab}}(\boldsymbol{\varphi}_h, \delta\boldsymbol{\varphi}) + \mathcal{W}_{\mathrm{T,stab}}(\mathbf{t}, \delta\mathbf{t}), \\ \forall\delta\boldsymbol{\Phi} = (\delta\boldsymbol{\varphi}, \delta\mathbf{t}) \in \mathbb{V}_h \end{aligned} \tag{48}$$

where the discrete counterparts

$$\bar{J}\mathbf{n}^\alpha = \frac{\partial\psi}{\partial(\partial_\alpha^{\mathrm{DG}}\boldsymbol{\varphi}_h)} \qquad \bar{J}\mathbf{l} = \frac{\partial\psi}{\partial\mathbf{t}_h} \qquad \bar{J}\mathbf{m}^\alpha = \frac{\partial\psi}{\partial(\partial_\alpha^{\mathrm{DG}}\mathbf{t}_h)} \tag{49}$$

of the stress resultant relations (9) have been used. Stable equilibrium positions may be found by searching for stationary points that are local minima.

Note that the minimization approach can be extended beyond elasticity to materials with dissipative behavior by recourse to *variational constitutive updates* [38]. In this technique, an incremental functional would take the place of (45). Alternatively, the variational viewpoint can be abandoned, and (48) may be regarded as the definition of a DG weighted residual weak form of the equilibrium equations.

3.7. Iterative solution procedure

The equilibrium problem can be solved iteratively with Newton's method by linearizing the virtual work about the current state in the direction of another set of admissible variations. Writing $\Delta\boldsymbol{\Phi} := (\Delta\mathbf{u}, \Delta\mathbf{t}) \in \mathbb{V}_h$, the weak form (48) is linearized again to yield

$$\langle DJ_h(\boldsymbol{\Phi}), \delta\boldsymbol{\Phi}\rangle + \left\langle D^2J_h(\boldsymbol{\Phi}), \delta\boldsymbol{\Phi}, \Delta\boldsymbol{\Phi}\right\rangle = 0, \quad \forall\delta\boldsymbol{\Phi} \in \mathbb{V}_h$$

which is solved for $\Delta\boldsymbol{\Phi}$ as a correction toward an improved guess.

The second variation of the discrete energy functional produces the bilinear form of the method $B_h : \mathbb{V}_h \times \mathbb{V}_h \to \mathbb{R}$,

$$B_h\left(\delta\boldsymbol{\Phi}, \Delta\boldsymbol{\Phi}\right) := \left\langle D^2J_h(\boldsymbol{\Phi}_h), \delta\boldsymbol{\Phi}, \Delta\boldsymbol{\Phi}\right\rangle$$

Symmetry of the bilinear form is guaranteed, as the second variation of a scalar potential is always symmetric. The stiffness matrix, being the representation of the bilinear form in the chosen basis, inherits this property. The bilinear form is naturally decomposed into three parts

$$B_h\left(\delta\boldsymbol{\Phi}, \Delta\boldsymbol{\Phi}\right) = B_h^{\mathrm{M}}\left(\delta\boldsymbol{\Phi}, \Delta\boldsymbol{\Phi}\right) + B_h^{\mathrm{G}}\left(\delta\boldsymbol{\Phi}, \Delta\boldsymbol{\Phi}\right) + B_h^{\mathrm{stab}}\left(\delta\boldsymbol{\Phi}, \Delta\boldsymbol{\Phi}\right)$$

where the superscripts are meant to suggest a material part, a geometric part, and a stabilization part. Each part if given in the following.

The material part of the bilinear form is recorded here under the assumption that the mixed second partial derivatives of the free energy with respect to $a_{\alpha\beta}$, γ_α, and $\kappa_{\alpha\beta}$ vanish. This restriction is typically obeyed by shell constitutive models for elastic, isotropic materials. Deriving the more general case leads to lengthy equations but is straightforward. With this proviso, the material part is given by

$$\begin{aligned} B_h^{\mathrm{M}}\left(\delta\boldsymbol{\Phi}, \Delta\boldsymbol{\Phi}\right) = \int_{\mathcal{S}_h^0} \Bigg[& \frac{\partial^2\psi}{\partial a_{\alpha\beta}\partial a_{\gamma\delta}}(\partial_\beta^{\mathrm{DG}}\delta\boldsymbol{\varphi}\cdot\mathbf{a}_\alpha + \partial_\alpha^{\mathrm{DG}}\delta\boldsymbol{\varphi}\cdot\mathbf{a}_\beta)(\partial_\gamma^{\mathrm{DG}}\Delta\mathbf{u}\cdot\mathbf{a}_\delta + \partial_\delta^{\mathrm{DG}}\Delta\mathbf{u}\cdot\mathbf{a}_\gamma) \\ & + \frac{\partial^2\psi}{\partial\gamma_\alpha\partial\gamma_\beta}(\partial_\alpha^{\mathrm{DG}}\delta\boldsymbol{\varphi}\cdot\mathbf{t}_h + \mathbf{a}_\alpha\cdot\delta\mathbf{t})(\partial_\beta^{\mathrm{DG}}\Delta\mathbf{u}\cdot\mathbf{t}_h + \mathbf{a}_\beta\cdot\Delta\mathbf{t}) \\ & + \frac{\partial^2\psi}{\partial\kappa_{\alpha\beta}\partial\kappa_{\gamma\delta}}(\partial_\alpha^{\mathrm{DG}}\delta\boldsymbol{\varphi}\cdot\mathbf{b}_\beta + \mathbf{a}_\alpha\cdot\partial_\beta^{\mathrm{DG}}\delta\mathbf{t})(\partial_\gamma^{\mathrm{DG}}\Delta\mathbf{u}\cdot\mathbf{b}_\delta + \mathbf{a}_\gamma\cdot\partial_\delta^{\mathrm{DG}}\Delta\mathbf{t})\Bigg]\, \bar{J}d\mathcal{S}^0 \end{aligned} \tag{50}$$

where $\mathbf{a}_\alpha = \partial_\alpha^{\mathrm{DG}} \boldsymbol{\varphi}_h$ and $\mathbf{b}_\alpha = \partial_\alpha^{\mathrm{DG}} \mathbf{t}_h$.

The geometric part of the bilinear form is

$$B_h^{\mathrm{G}}(\delta\boldsymbol{\Phi}, \Delta\boldsymbol{\Phi}) = \int_{\mathcal{S}_h^0} \Big[\widetilde{n}^{\alpha\beta} (\partial_\alpha^{\mathrm{DG}} \delta\boldsymbol{\varphi} \cdot \partial_\beta^{\mathrm{DG}} \Delta\mathbf{u} + \partial_\beta^{\mathrm{DG}} \delta\boldsymbol{\varphi} \cdot \partial_\alpha^{\mathrm{DG}} \Delta\mathbf{u}) + \widetilde{q}^{\alpha} (\partial_\alpha^{\mathrm{DG}} \delta\boldsymbol{\varphi} \cdot \Delta\mathbf{t} + \partial_\alpha^{\mathrm{DG}} \Delta\mathbf{u} \cdot \delta\mathbf{t}) + \widetilde{m}^{\alpha\beta} (\partial_\alpha^{\mathrm{DG}} \delta\boldsymbol{\varphi} \cdot \Delta \partial_\beta^{\mathrm{DG}} \mathbf{t} + \partial_\alpha^{\mathrm{DG}} \Delta\mathbf{u} \cdot \delta \partial_\beta^{\mathrm{DG}} \mathbf{t}) \Big] \bar{J} d\mathcal{S}^0 \tag{51}$$

Finally, the stabilization part is

$$B_h^{\mathrm{stab}}(\delta\boldsymbol{\Phi}, \Delta\boldsymbol{\Phi}) = \mathcal{W}_{\mathrm{x,stab}}(\delta\boldsymbol{\varphi}, \Delta\mathbf{u}) + \mathcal{W}_{\mathrm{T,stab}}(\delta\mathbf{t}, \Delta\mathbf{t}) \tag{52}$$

Substitution of the basis for $\mathbb{V}_h$ into the bilinear form leads to the definition of the stiffness matrix in the standard way:

$$B_h(\delta\boldsymbol{\Phi}, \Delta\boldsymbol{\Phi}) = [\mathbf{v}]^\top [\mathbf{K}] [\mathbf{u}],$$

where $[\mathbf{K}]$ is the global stiffness matrix, and $[\mathbf{u}]$ and $[\mathbf{v}]$ are column vectors of the nodal values of the corrections and the variations. Explicit equations for the elemental stiffness matrices are given in Appendix A.

As an aside, since $\Delta\mathbf{u} \in \boldsymbol{V}_h$ and $\Delta\mathbf{t} \in T_{\mathbf{t}_h} \boldsymbol{T}_h$, it is evident that the simplest element in the family, $k = 2$, has 6 displacement nodes, with 3 degrees of freedom each, and 3 director nodes, each with 2 degrees of freedom, for a total of 24 degrees of freedom.

3.8. Kinematic update

Each iteration of Newton's method yields linearized corrections that must be applied to update the configuration of the shell. The geometry of the director manifold must be considered carefully to keep the nodal directors in the unit sphere. At Newton iterate k, the current nodal unknowns $(\mathbf{x}_A^k, \mathbf{t}_A^k)$ must be updated with the linear correction $(\Delta\mathbf{u}_A, \Delta\mathbf{T}_A)$ to yield the improved guess $(\mathbf{x}_A^{k+1}, \mathbf{t}_A^{k+1})$.

The mid-surface displacements are vectors, and so the update is achieved trivially by adding the corrections. The nodal directors $\mathbf{t}_A \in S^2$, however, are updated using the exponential map on the unit sphere. Remarkably, this can be written in closed form. This update procedure was determined by Simo et al. [36], and is given in Algorithm 1. This algorithm is geometrically exact, and well-conditioned under nonzero corrections of arbitrary size.

3.9. Specialization to linearized kinematics

In this section, the finite element method described above is linearized about the reference configuration to yield the linear kinematic version. A set of admissible variations about the reference configurations can be found by taking the curves

$$\begin{aligned} \boldsymbol{\varphi}_\varepsilon &= \boldsymbol{\varphi}^0 + \varepsilon \mathbf{u} \\ \mathbf{t}_\varepsilon &= \cos \|\varepsilon \Delta\mathbf{t}\| \, \mathbf{t}^0 + \frac{\sin \|\varepsilon \Delta\mathbf{t}\|}{\varepsilon \Delta\mathbf{t}} \varepsilon \Delta\mathbf{t} \end{aligned}$$

Thus, the linearized displacements are $(\mathbf{u}_h, \Delta\mathbf{t}_h) \in \boldsymbol{X}_h \times T_{\mathbf{t}^0} \boldsymbol{T}_h$. This leads to the definition of the linearized strains

$$\epsilon_{\alpha\beta} = \frac{1}{2} \left(\partial_\alpha \boldsymbol{\varphi}^0 \cdot \partial_\beta^{\mathrm{DG}} \mathbf{u}_h + \partial_\beta \boldsymbol{\varphi}^0 \cdot \partial_\alpha^{\mathrm{DG}} \mathbf{u}_h \right) \tag{56}$$

$$\zeta_\alpha = \partial_\alpha^{\mathrm{DG}} \mathbf{u}_h \cdot \mathbf{t}^0 + \partial_\alpha \boldsymbol{\varphi}^0 \cdot \Delta\mathbf{t}_h \tag{57}$$

$$\rho_{\alpha\beta} = \partial_\alpha^{\mathrm{DG}} \mathbf{u}_h \cdot \partial_\beta \mathbf{t}^0 + \partial_\alpha \boldsymbol{\varphi}^0 \cdot \partial_\beta^{\mathrm{DG}} \Delta\mathbf{t}_h \tag{58}$$

With an abuse of notation, the linearized strains are written with the same symbols as in the hyperelastic model in Section 2.5.

Algorithm 1 Kinematic update procedure.

1: Update nodal positions

$$\mathbf{x}_A^{k+1} = \mathbf{x}_A^k + \Delta\mathbf{u}_A$$

2: Compute spatial director increments

$$\Delta\mathbf{t}_A = \bar{\mathbf{\Lambda}}_A^k \Delta\mathbf{T}_A$$

3: Update directors with exponential map

$$\mathbf{t}_A^{k+1} = \exp_{\mathbf{t}_A^k}(\Delta\mathbf{t}_A) := \cos\|\Delta\mathbf{t}_A\|\,\mathbf{t}_A^k + \frac{\sin\|\Delta\mathbf{t}_A\|}{\|\Delta\mathbf{t}_A\|}\Delta\mathbf{t}_A \tag{53}$$

4: Compute rotation increment

$$\Delta\mathbf{\Lambda}_A = \cos\|\Delta\mathbf{t}_A\|\,\mathbf{1} + \frac{\sin\|\Delta\mathbf{t}_A\|}{\|\Delta\mathbf{t}_A\|}(\mathbf{t}_A^k \times \widehat{\Delta\mathbf{t}}_A) + \frac{1-\cos\|\Delta\mathbf{t}_A\|}{\|\Delta\mathbf{t}_A\|^2}(\mathbf{t}_A^k \times \Delta\mathbf{t}_A)\otimes(\mathbf{t}_A^k \times \Delta\mathbf{t}_A) \tag{54}$$

5: Update rotations

$$\mathbf{\Lambda}_A^{k+1} = \Delta\mathbf{\Lambda}_A\mathbf{\Lambda}_A^k \tag{55}$$

Linearizing the potential energy functional in the direction of the variations defined above yields

$$\begin{aligned} J_h^0(\mathbf{u}_h, \Delta\mathbf{t}_h) = &\int_{\mathcal{S}_h}\left(\frac{1}{2}tH^{\alpha\beta\gamma\delta}\epsilon_{\alpha\beta}\epsilon_{\gamma\delta} + \frac{1}{2}k\mu t a^{0\alpha\beta}\zeta_\alpha\zeta_\beta + \frac{1}{2}\frac{t^3}{12}H^{\alpha\beta\gamma\delta}\rho_{\alpha\beta}\rho_{\gamma\delta}\right)d\mathcal{S} - \mathcal{W}_{\text{ext}}(\mathbf{u}_h, \Delta\mathbf{t}_h) \\ &+ \frac{1}{2}\int_{\Gamma_I}\left(\frac{\beta_x}{h^e}[\![\mathbf{u}_h]\!]\cdot[\![\mathbf{u}_h]\!] + \frac{\beta_T}{h^e}[\![\Delta\mathbf{t}_h]\!]\cdot[\![\Delta\mathbf{t}_h]\!]\right)\bar{j}ds \end{aligned}$$

The previous definition of the elastic tensor is retained. The stiffness matrix for the linearized method can be found by taking the fully nonlinear stiffness matrix in Appendix A and eliminating the geometric stiffness terms. As is standard, there is no distinction between the reference and current configurations in the linear theory. As a consequence, the update formula in Algorithm 1 is disregarded.

4. Implementation

A strategy to implement the weak form in (48) in a standard finite element code is given in this section. In our implementation, calculation of the shape function data is handled through the `Gmsh` mesh processing library [39]. The `Gmsh` library also provides geometric information and adjacency relationships of the triangulation that are convenient for implementing DG methods.

4.1. Discretization of the lifting operator

The DG derivative operator is applied by pre-computing and storing the action of the lifting operator on the basis functions of the kinematic fields. The details of this computation are recorded in this section. It is shown that the representation of the lifting operator is of the same form as the familiar shape function derivatives, and thus can be stored in a similar data structure.

The DG derivative is taken with respect to the *convected coordinates*, and thus the formulation of the DG derivative in Section 3.4 involves integrals over the parameterization space. This is somewhat different than typical discontinuous Galerkin methods, where the ambient space and the manifold of the domain are both the same Euclidean space, and the DG derivative is taken with respect to a Cartesian coordinate system.

Of course, the parameterization space for every element is identical, in the sense that each element maps from a copy of the master element according to the isoparametric approach. The upshot is that the lifting operator can be computed once and for all on the master element in the convected coordinates $\{\xi^1, \xi^2\}$ and used to compute the DG derivative on every $E \in \mathcal{T}_h$.

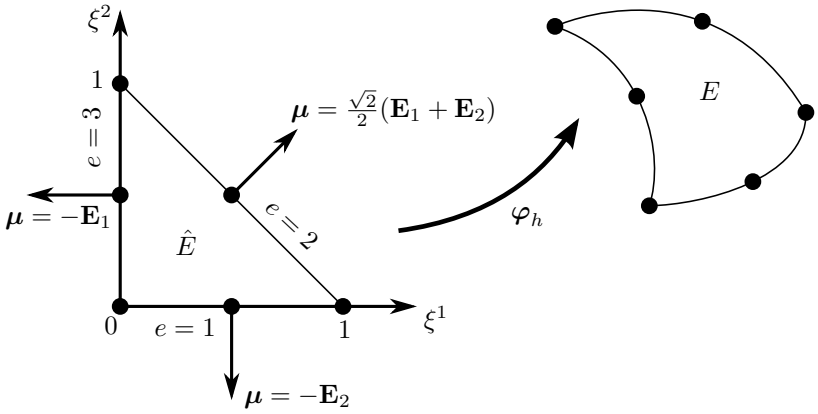

Figure 3: The master element used for $\mathcal{P}_2(E)$, showing the unit normals to each edge.

For $\boldsymbol{\psi} \in \boldsymbol{X}_h$, the lifting operator within element E is defined by (35)

$$\int_{\hat{E}} \mathbf{r}_\alpha(\boldsymbol{\psi}) \cdot \mathbf{z}^\alpha \, d\mathcal{A} = -\int_{\partial\hat{E}} \boldsymbol{\psi} \{\mathbf{z}^\alpha\} \, \mu_\alpha \, ds, \quad \forall \mathbf{z}^\alpha \in \boldsymbol{W}_h^E$$

The boundary of the master element $\partial\hat{E}$ can be partitioned into its three edges. The lifting operator can be decomposed into contributions from each edge, leading to the definition of the edge lifting operator $\mathbf{r}_\alpha^e \colon [L^2(\Gamma_I)]^3 \to \boldsymbol{W}_h^E$,

$$\int_{\hat{E}} \mathbf{r}_\alpha^e(\boldsymbol{\psi}) \cdot \mathbf{z}^\alpha \, d\mathcal{A} = -\int_e \boldsymbol{\psi} \{\mathbf{z}^\alpha\} \, \mu_\alpha \, ds, \quad \forall \mathbf{z}^\alpha \in \boldsymbol{W}_h^E \tag{59}$$

Clearly $\mathbf{r}_\alpha = \sum_{e \in \Gamma_I} \mathbf{r}_\alpha^e$.

Inserting the representation of $\boldsymbol{\psi}$ in the chosen basis of X_h, and then making use of the linearity of the lifting operator allows one to write

$$\mathbf{r}_\alpha^e \left(\sum_A N^A \boldsymbol{\psi}_A \right) = \sum_A r_\alpha^e(N^A) \boldsymbol{\psi}_A$$

The action of the edge lifting operator on the basis functions of $\boldsymbol{X}_h$, $r_\alpha^e(N^A)$, is thus needed to compute the DG derivative. Let $[r^e]_\alpha^A := r_\alpha^e(N^A)$, and let Q^B denote the basis functions of W_h. Then (59) is written

$$\int_{\hat{E}} \left(\sum_B Q^B(\boldsymbol{\xi}) \sum_A [r^e]_{\alpha B}^A \boldsymbol{\psi}_A \right) \left(\sum_C Q^C(\boldsymbol{\xi}) \, \mathbf{z}_C^\alpha \right) d\mathcal{A} = \\ -\frac{1}{2} \int_e \left(\sum_A N^A(\boldsymbol{\xi}) \boldsymbol{\psi}_A \right) \left(\sum_C Q^C(\boldsymbol{\xi}) \mathbf{z}_C^\alpha \right) \mu_\alpha \, ds, \quad \forall \mathbf{z}^\alpha \in \boldsymbol{W}_h^E$$

Taking the sums outside the integrals, and then applying the standard variational arguments, the above holds independently for every $\mathbf{z}_C^\alpha$ and $\boldsymbol{\psi}_A$ so that

$$\sum_B [r^e]_{\alpha B}^A \int_{\hat{E}} Q^B Q^C \, d\mathcal{A} = -\frac{1}{2} \int_e N^A Q^C \mu_\alpha \, ds$$

The integral on the left hand side is recognized as the components of the elemental mass matrix for W_h^E,

$$[M^{\hat{E}}]^{BC} := \int_{\hat{E}} Q^B Q^C \, d\mathcal{A}.$$

Defining the notation

$$[G^e]_\alpha^{AC} := \int_e N^A Q^C \mu_\alpha \, ds,$$

the nodal values of the edge lifting operator are found simply by solving the linear system

$$\sum_B [M^{\hat{E}}]^{BC} [r^e]_{\alpha B}^A = -\frac{1}{2} G_\alpha^{AC} \tag{60}$$

for each $A \in e$ and $\alpha \in \{1, 2\}$. The mass matrix $[M^{\hat{E}}]^{BC}$ is symmetric and positive definite, and hence invertible. This system is small, as the elemental mass matrix has rows and columns of size $\dim W_h^E$; note that this size depends only on the polynomial degree chosen for W_h^E and is independent of the global problem size.

With the nodal values computed, the edge lifting can be interpolated to any point in the master element. Expanding the lifting in the basis for W_h gives

$$[r^e]_\alpha^A(\boldsymbol{\xi}) := \sum_B Q^B(\boldsymbol{\xi}) [r^e]_{\alpha B}^A \tag{61}$$

This shows that the lifting operator representation $[r^e]_\alpha^A$ has the same form as the derivatives of the primal shape functions $\partial_\alpha N^A(\boldsymbol{\xi})$. This fact can be exploited to store the lifting operator at the quadrature points of the element in a manner that is compatible with existing finite element codes.

Using the procedure above, the DG derivative of the position map is computed according to

$$\begin{aligned} \partial_\alpha^{\mathrm{DG}} \boldsymbol{\varphi}_h &= \partial_{h\alpha} \boldsymbol{\varphi}_h + \mathbf{r}_\alpha([\![\boldsymbol{\varphi}_h]\!]) \\ &= \sum_{A=1}^{n_x} \partial_\alpha N^A \bar{\mathbf{x}}_A \pm \sum_{e \in \partial \hat{E}} \sum_{A=1}^{ne_x} [r^e]_\alpha^A \bar{\mathbf{x}}_A \end{aligned} \tag{62}$$

The positive sign is used for the degrees of freedom on the edge e belonging to the current element, and the negative sign is taken for degrees of freedom on the edge belonging to the neighbor element. (With the strong enforcement of boundary conditions, the lifting operator vanishes on edges on the essential boundary of the domain, and thus these edges are omitted in the summation over e).

The lifting operator of the director field is computed in an analogous way. The corresponding DG derivative is written

$$\partial_\alpha^{\mathrm{DG}} \mathbf{t}_h = \sum_{A=1}^{n_T} \partial_\alpha L^A \mathbf{t}_A \pm \sum_{e=1}^{3} \sum_{A=1}^{ne_T} [\mathbf{r}^e]_\alpha^A \mathbf{t}_A \tag{63}$$

It is emphasized that the polynomial degree of the derivative approximation spaces W_h and K_h affects only the size of the pre-processing problem (60), and does not affect the number of unknowns or the matrix bandwidth in the global problem.

4.2. Element internal forces

As in standard finite element method implementations, the nodal forces and stiffness matrix are assembled element by element. The internal nodal forces are given in this section in explicit form amenable to computer

implementation. The internal virtual work can be rewritten as a sum of elemental contributions in the form

$$\mathcal{W}_{\text{int}}(\boldsymbol{\varphi}_h, \mathbf{t}_h; \delta\boldsymbol{\varphi}, \delta\mathbf{t}) = \sum_{E\in\mathcal{T}_h} \sum_{A\in C_x^E} [\mathbf{f}^E_{\text{x,int}}]^A \cdot \delta\bar{\mathbf{x}}_A + \sum_{E\in\mathcal{T}_h} \sum_{A\in C_T^E} [\mathbf{f}^E_{\text{T,int}}]^A \cdot \delta\mathbf{T}_A$$

where C_x^E and C_T^E are sets of nodes defined shortly.

Substituting the interpolations into the internal virtual work shows that the nodal forces appearing in the above are

$$[\mathbf{f}^E_{\text{x,int}}]^A = \int_E \mathbf{n}^\alpha \left(\partial_\alpha N^A \pm \sum_{e=1}^{3} [r^e]^A_\alpha \right) \bar{J} d\mathcal{S}^0 \tag{64}$$

$$[\mathbf{f}^E_{\text{T,int}}]^A = \int_E (\bar{\boldsymbol{\Lambda}}^A)^\top \mathbf{m}^\alpha \left(\partial_\alpha L^A \pm \sum_{e=1}^{3} [\mathbf{r}^e]^A_\alpha \right) \bar{J} d\mathcal{S}^0 + \int_E (\bar{\boldsymbol{\Lambda}}^A)^\top \mathbf{l}\, L^A \, \bar{J} d\mathcal{S}^0 \tag{65}$$

Note that $[\mathbf{f}^E_{\text{T,int}}]^A$, the nodal forces paired to the nodal director variations have *two components*.

At this point C_x^E and C_T^E may be easily identified. Since the edge lifting operates on the kinematic jumps at the element boundaries, all of the nodes inside the dashed circle in Figure 4 are needed to compute the DG derivative in the shaded element.[4] Thus $\#C_x^E = n_x + 3ne_x$ and $\#C_T^E = n_T + 3ne_T$. Due to the reciprocity guaranteed by the variational principle, the extended node sets C_x^E and C_T^E are needed to compute the strains inside the shaded element, and in turn, forces are generated on each of these nodes. It is interesting that the use of an extended set of degrees of freedom bears some similarity to subdivision shell elements [40, 41, 42]. However, discontinuous Galerkin methods only couple degrees of freedom through face adjacencies; no coupling is induced between elements sharing only vertices. The maximum number of nonzero elements per row in the stiffness matrix is thus bounded. Furthermore, if all degrees of freedom belonging to an element are numbered consecutively, the stiffness matrix has a block structure, where the number of nonzero blocks in each row is known a priori (apart from boundary degrees of freedom). This predictable structure may be exploited to design efficient factorization schemes for direct solvers or preconditioners (see, e.g., [43]). Another advantage of this structure is that common element-level operations, such as interpolation of the kinematic fields and the nodal force assembly in (64) and (65), use values largely stored in contiguous blocks of memory.

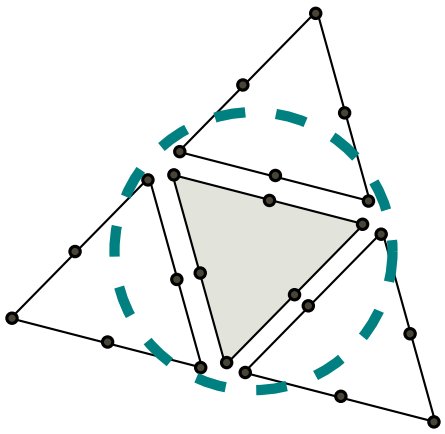

Figure 4: Degrees of freedom needed to compute DG derivative on the grey element.

[4] This requirement holds for the nodes in the displacement interpolation and the nodes in the director interpolation.

Regarding the representation of the nodal unknowns: the material director increments are naturally stored as components of $\mathbb{R}^2$, that is, $\Delta\mathbf{T}_A = \Delta T_A^\alpha \mathbf{E}_\alpha$; it is recommended that the displacement increments be stored relative to the fixed Cartesian basis of the ambient space $\mathbb{R}^3$, that is, $\Delta\mathbf{u}_A = u_A^i \mathbf{E}_i$. In order to reduce the matrix bandwidth and to promote usage of contiguous memory blocks, it is recommended that the displacement and director correction unknowns are numbered together element-wise, and that the spatial components of each unknown are indexed consecutively.

The integrals in (64) and (65) are computed approximately with a quadrature rule. For stiffness and residual calculations, the selection of the quadrature rule is made using the Reissner plate system as a guide. The highest degree term appearing in the Reissner virtual work is a polynomial of degree $2k-2$; the quadrature rule of the shell element is selected to achieve at least this level of precision.

A step-by-step procedure for computing the internal forces in an element is given in Algorithm 2.

Algorithm 2 Computation of the internal nodal forces.

1: Interpolate $\boldsymbol{\varphi}_h$ and $\mathbf{t}_h$ according to (20) and (21):

$$\boldsymbol{\varphi}_h = \sum_A^{n_x} N^A \bar{\mathbf{x}}_A \qquad\qquad \mathbf{t}_h = \sum_A^{n_T} L^A \mathbf{t}_A$$

2: Compute the DG derivatives $\partial_\alpha^{\mathrm{DG}} \boldsymbol{\varphi}_h$ and $\partial_\alpha^{\mathrm{DG}} \mathbf{t}_h$ using (62) and (63):

$$\partial_\alpha^{\mathrm{DG}} \boldsymbol{\varphi}_h = \sum_{A=1}^{n_x} \partial_\alpha N^A \bar{\mathbf{x}}_A \pm \sum_{e=1}^{3} \sum_{A=1}^{ne_x} [r^e]_\alpha^A \bar{\mathbf{x}}_A$$
$$\partial_\alpha^{\mathrm{DG}} \mathbf{t}_h = \sum_{A=1}^{n_T} \partial_\alpha L^A \mathbf{t}_A \pm \sum_{e=1}^{3} \sum_{A=1}^{ne_T} [\mathbf{r}^e]_\alpha^A \mathbf{t}_A$$

3: Compute $a_{\alpha\beta}, \gamma_\alpha, \kappa_{\alpha\beta}$:

$$a_{\alpha\beta} = \partial_\alpha^{\mathrm{DG}} \boldsymbol{\varphi}_h \cdot \partial_\beta^{\mathrm{DG}} \boldsymbol{\varphi}_h$$
$$\gamma_\alpha = \partial_\alpha^{\mathrm{DG}} \boldsymbol{\varphi}_h \cdot \mathbf{t}_h$$
$$\kappa_{\alpha\beta} = \partial_\alpha^{\mathrm{DG}} \boldsymbol{\varphi}_h \cdot \partial_\beta^{\mathrm{DG}} \mathbf{t}_h$$

4: Apply the constitutive laws (11): $(a_{\alpha\beta}, \gamma_\alpha, \kappa_{\alpha\beta}; a^0_{\alpha\beta}, \gamma^0_\alpha, \kappa^0_{\alpha\beta}) \mapsto (\widetilde{n}^{\alpha\beta}, \widetilde{q}^\alpha, \widetilde{m}^{\alpha\beta})$

5: Collect $\mathbf{n}^\alpha, \mathbf{m}^\alpha, \mathbf{l}$ according to (10):

$$\mathbf{n}^\alpha = \widetilde{n}^{\alpha\beta} \partial_\beta \boldsymbol{\varphi} + \widetilde{m}^{\alpha\beta} \partial_\beta \mathbf{t} + \widetilde{q}^\alpha \mathbf{t}$$
$$\mathbf{l} = \widetilde{q}^\alpha \partial_\alpha \boldsymbol{\varphi}$$
$$\mathbf{m}^\alpha = \widetilde{m}^{\alpha\beta} \partial_\alpha \boldsymbol{\varphi}$$

6: Compute the nodal internal forces using (64) and (65).

4.3. Stabilization internal forces

The internal forces arising from the stability terms are assembled from each interface element. The virtual work from the stability terms is written

$$\mathcal{W}_{\text{x,stab}}(\boldsymbol{\varphi}_h, \delta\boldsymbol{\varphi}) = \sum_{e\in\Gamma_I}\sum_{A=1}^{ne_x} [\mathbf{f}^E_{\text{x,stab}}]^A \cdot \delta\bar{\mathbf{x}}_A$$

$$\mathcal{W}_{\text{T,stab}}(\mathbf{t}_h, \delta\mathbf{t}) = \sum_{e\in\Gamma_I}\sum_{A=1}^{ne_t} [\mathbf{f}^E_{\text{T,stab}}]^A \cdot \delta\mathbf{T}_A$$

The nodal forces are thus

$$[\mathbf{f}^e_{\text{x,stab}}]^A = \pm\int_e \frac{\beta_x}{h^e}\,[\![\boldsymbol{\varphi}_h]\!]\,N^A\,\bar{j}^0 ds \tag{66}$$

$$[\mathbf{f}^e_{\text{T, stab}}]^A = \pm\int_e (\bar{\boldsymbol{\Lambda}}^A)^\top \frac{\beta_T}{h^e}\,[\![\mathbf{t}_h]\!]\,L^A\,\bar{j}^0 ds \tag{67}$$

which are common to many DG methods, apart from the appearance of the nodal rotation matrix $\boldsymbol{\Lambda}^A$.

5. Examples

In this section, a numerical implementation of the proposed method is subjected to a set of benchmarks and examples. In all problems, solution of the systems of equations is performed through the `PETSc` scientific computing library [44] using the LU and Cholesky direct solver routines.

The quadratic element $k = 2$ is used in all examples. The nodal points in the interpolations are illustrated in Figure 5. The issue of choosing the stabilization parameters optimally is not examined in detail here; however, the method was found to be rather insensitive to the stabilization parameters, and taking $c_x, c_T \in [1, 10]$ was found to be sufficient. An adaptive stabilization scheme as in [45] could be a useful development in the future.

(a) (b)

Figure 5: Node locations for $k = 2$ element for (a) the displacement interpolation and (b) the director interpolation

5.1. Linear benchmarks

In this section, the accuracy of the proposed method with linearized kinematics is assessed with published linear benchmarks. Even in the restricted scope of linear problems, analyzing the accuracy of numerical methods for shells is surprisingly difficult. For the most part, exact solutions are not known, and thus measuring convergence rigorously in terms of norms is not possible. Most researchers and practicing engineers largely rely on heuristic benchmarks to assess shell methods. Unfortunately, the most commonly used benchmarks only test point-wise convergence of displacement or forces, and are not necessarily indicative of the relative performance of different methods. Furthermore, many of the benchmark problems lack sufficient regularity to be well-posed for shear-flexible shells: in particular, point loads are inadmissible in these

theories. These shortcomings have been recognized over the last 20 years, and mathematical analysis has been done to shed light on the inherent difficulties; in particular, the work Pitkäranta and co-workers [46, 47] and Bathe and Chapelle [48, 49, 50] deserve mention. Reference [46] notes that in the limit of vanishing thickness, well-posed shell problems range between two limiting regimes: (i) bending dominated problems and (ii) membrane dominated problems. This suggests that if a method is able to function accurately and efficiently (without locking) in both extremes, it is likely to be successful.

5.2. Patch tests

Membrane and bending patch tests were performed to verify that constant strain fields are exactly reproduced by the element. Both tests were conducted on a domain of the unit square in the xy-plane. The mesh used for these tests is shown in Figure 6. The parameters of the problems are the plate edge length L, the plate thickness t, the Young's modulus E, and the Poisson's ratio ν.

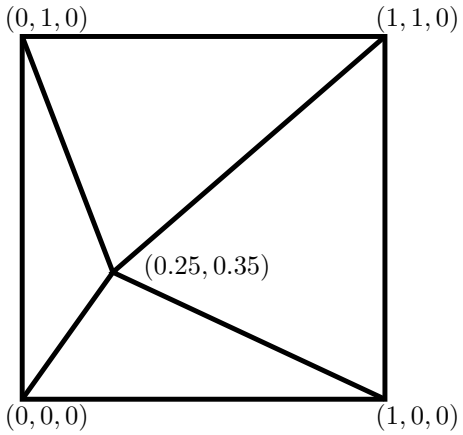

Figure 6: Geometry of the mesh used in the patch tests.

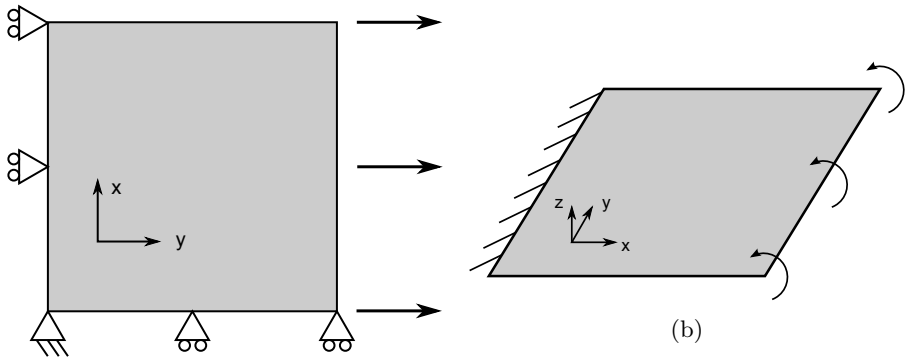

Figure 7: Patch test configurations. (a) Membrane test. Out-of-plane displacements are constrained on left and bottom edges (not shown in figure). (b) Bending test.

In both problems, the implementation of the proposed method was verified to satisfy the above solutions exactly at every nodal point (within machine precision).

5.3. Clamped plate problem of Chinosi and Lovadina plate bending

In this section, the convergence of the proposed method is evaluated numerically on the clamped plate problem of Chinosi and Lovadina [51]. The convergence is measured over a range of plate thicknesses in

order to check for locking in the thin plate limit. Ideally, the numerical solution should converge uniformly as a function of thickness.

The problem is defined on a plate occupying the unit square, which is clamped on all sides. The plate is subjected to the load $\mathbf{f} = f_3\mathbf{E}_3$, with

$$f_3(x,y) = \frac{Et^3}{12(1-\nu^2)}\Big[12y(y-1)(5x^2-5x+1)\left(2y^2(y-1)^2+x(x-1)(5y^2-5y+1)\right) \\ + 12x(x-1)(5y^2-5y+1)\left(2x^2(x-1)^2+y(y-1)(5x^2-5x+1)\right)\Big].$$

The load contains a scale factor of t^3 so that the displacement converges to a finite limit as $t \to 0$. The exact solution of the displacement field is

$$u_3(x,y) = \frac{1}{3}x^3(x-1)^3y^3(y-1)^3 \\ - \frac{2t^2}{5(1-\nu)}\left[y^3(y-1)^3x(x-1)(5x^2-5x+1)x^3(x-1)^3y(y-1)(5y^2-5y+1)\right]$$

The first term is the Kirchhoff thin plate limit solution, while the second term represents the Reissner theory correction, which decays as $O(t^2)$. The rotation field solution is

$$-\Delta t_1 = \theta_1(x,y) = y^3(y-1)^3x^2(x-1)^2(2x-1)$$
$$-\Delta t_2 = \theta_2(x,y) = x^3(x-1)^3y^2(y-1)^2(2y-1)$$

where θ_α are the infinitesimal rotation components of Reissner-Mindlin theory.

The proposed plate method was exercised on this problem for $t/L = \{1, 10^{-1}, 10^{-2}, 10^{-3}\}$, where L is the plate edge length.[5] A uniform mesh of right triangles was used; each mesh refinement was performed by uniform subdivision. Error is measured with respect to the broken (element by element) H^s norms, $s = 0, 1$, which are indicated by $\|\bullet\|_{s,h}$. The results are shown in Figure 8. In each plot, the optimal rate of convergence with respect to the mesh diameter h in the corresponding norm is indicated by a grey triangle. In each case, the optimal convergence rate is met, for every plate thickness.

Furthermore, the error for normalized plate thicknesses between 1 and 10^{-2} have converged to the *same* asymptotic behavior. The errors for the $t/L = 10^{-3}$ plate also appear to be approaching the same line, possibly requiring one or two more levels of refinement. (Further refinement was not practical on available computers). This is the expected behavior of a uniformly convergent method. These results attest to the robustness of the proposed DG method as a general plate analysis tool for both thick and thin plates.

5.4. Clamped cylinder

This problem was suggested by Pitkäranta et al.[46] to test the convergence of a curved shell element in a membrane dominated problem. The problem consists of a cylinder with clamped ends, subjected to a pressure varying over the azimuth angle θ

$$\frac{p(\theta)}{p_0} = \frac{t}{R}\cos 2\theta$$

where p_0 is an arbitrarily chosen reference pressure, R is the cylinder radius, and t is the wall thickness. The other parameters of the problem are the cylinder length L, and the material parameters specified in Table 1.

[5] Clearly $t/L = 1$ is not physical, but including this range brackets most practical plate problems in terms of orders of magnitude, and allows us to assess the mathematical properties of the method from "thick" plates to "thin".

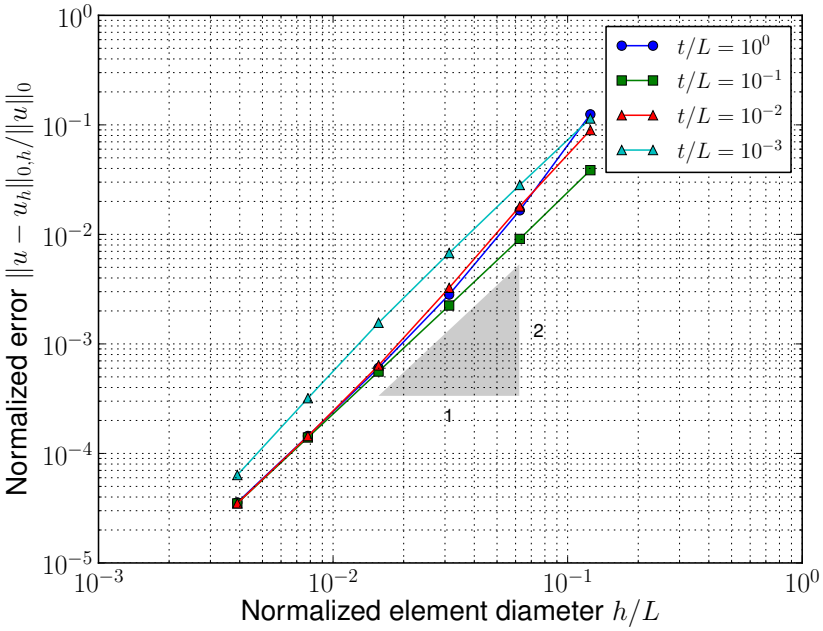

(a)

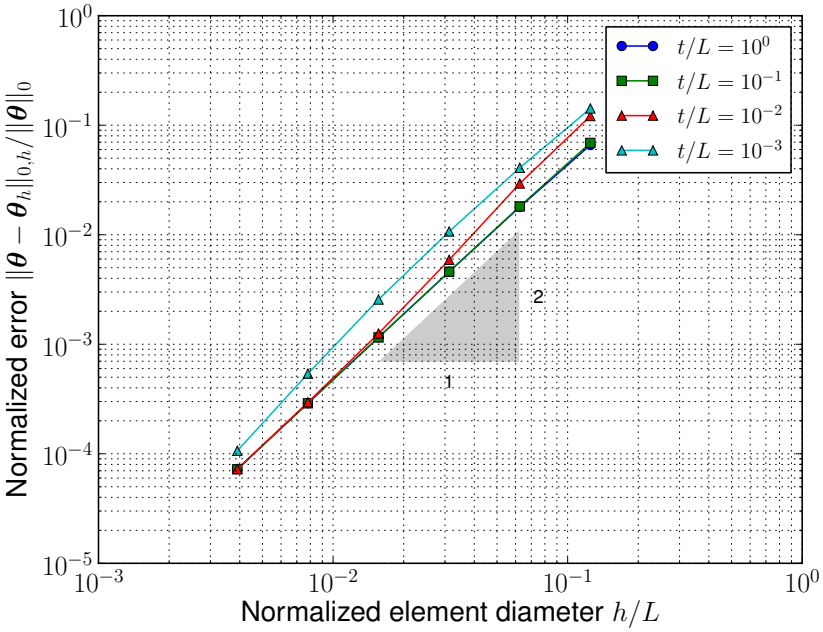

(b)

Figure 8: Error in the numerical solution from the proposed plate DG method in the clamped plate problem of Chinosi and Lovadina. The error is measured over a range of plate thicknesses to check for locking. The results suggestive the method is uniformly convergent. (a) Error in u_h in the L^2 norm. (b) Error in $\boldsymbol{\theta}_h$ in the L^2 norm. (c) Error in $\boldsymbol{\theta}_h$ in the broken H^1 norm.

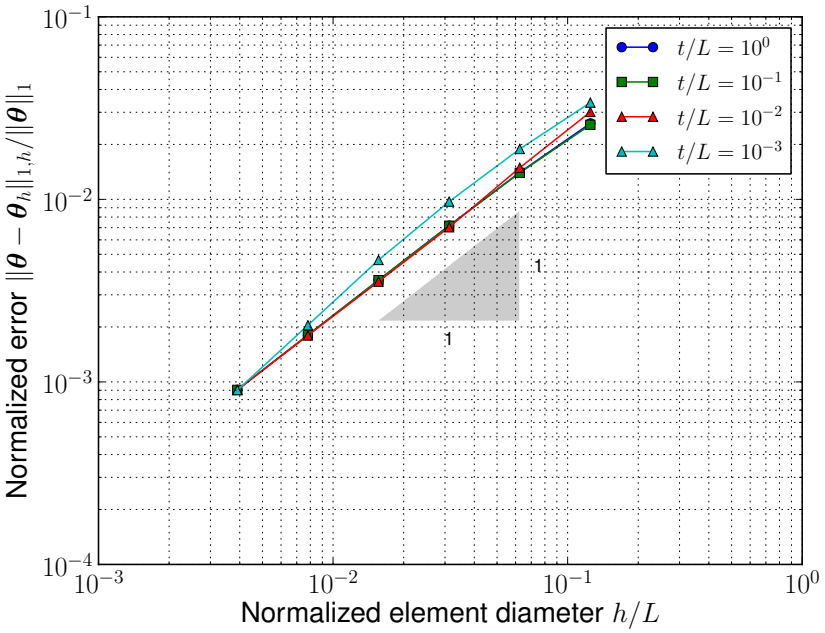

(c)

Table 1: Parameters for the clamped cylinder test.

Parameter	Symbol
E/p_0	200×10^3
ν	$1/3$
L/R	1
c_x	2
c_T	2

The convergence of the numerical method is measured with respect to an analytical calculation of the strain energy given in [46], and is repeated in Table 2.[6] The problem is solved on a sequence of regular meshes, with the first mesh in the refinement sequence shown in Figure 8. Successive meshes are obtained by uniform subdivision. In figure 9, the proposed DG method is compared with results obtained in [49] for several of the MITC shell elements, which are among the best performing elements known. The MITC6 element, being the quadratic triangle element of the family, is the closest relative of the $k = 2$ DG shell element tested here. In terms of the relative error in the strain energy, the present method is seen to be similar in performance to the MITC6 element. The accuracy level remains comparable as the shell becomes thin. The proposed method shows no tendency to lock in this membrane-dominated test.

Table 2: Exact solution of the strain energy for the clamped cylinder problem, from [46]. The energy is $C \times \dfrac{6p_0^2R^3(1-\nu^2)}{E}\dfrac{t}{R}$.

t/R	C
0.01	2.688287959059254
0.001	2.796612585420251

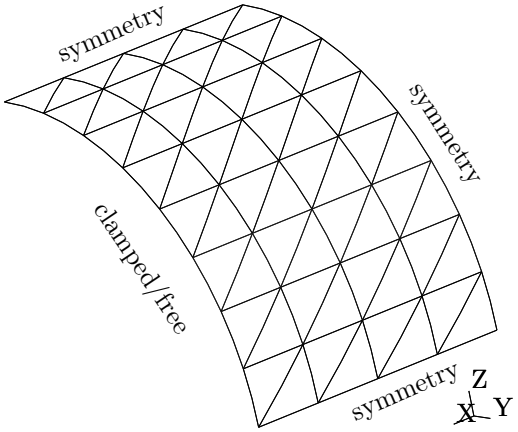

Figure 8: Coarsest mesh used in the clamped and free cylinder benchmarks. The other meshes in the sequence are created by uniform subdivision.

5.5. Free cylinder

This problem, another benchmark suggested by Pitkäranta et al.[46], tests curved shell elements in a bending-dominated problem. The cylinder mesh is subject only to the symmetry constraints, and the end is left free. The geometry, and properties, and meshes are identical to those in the clamped cylinder benchmark. The loading is given by

$$\frac{p(\theta)}{p_0} = \left(\frac{t}{R}\right)^3 \cos 2\theta.$$

The exact solution of the strain energy is given in Table 3.

The proposed method is again compared to the MITC elements in terms of relative error in strain energy. The results are shown in Figure 10. The proposed method again displays good convergence with mesh refinement. In the $t/R = 10^{-2}$ case, the accuracy is nearly identical to the MITC6 element. In the

[6] The reference energy given in [46] contains an error, and should be multiplied by $(1-\nu)^2$ [47].

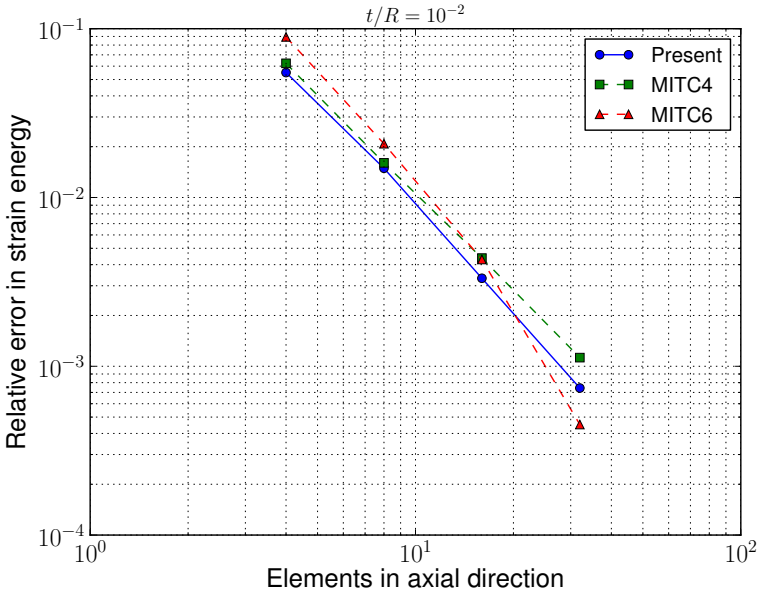

(a)

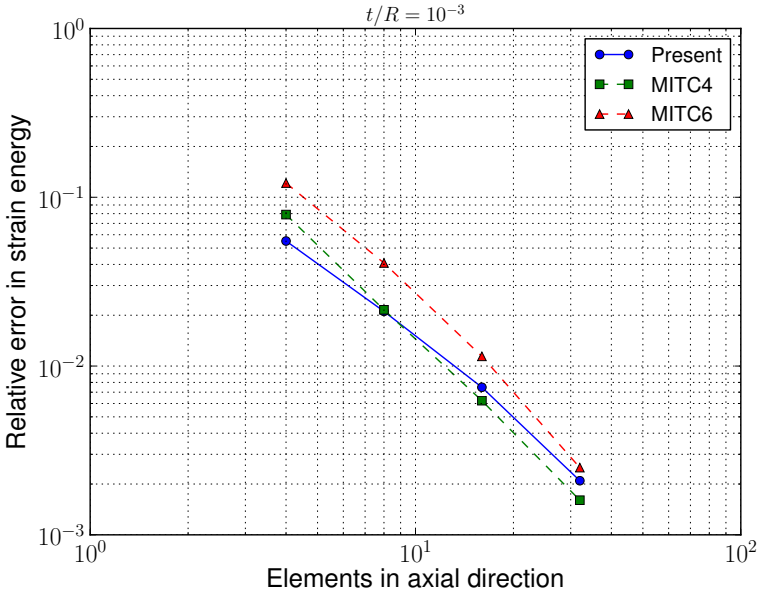

(b)

Figure 9: Relative error in strain energy in the clamped cylinder benchmark. Results plotted for current DG scheme as well as quadrilateral first order MITC elements (MITC4) and triangular second order MITC elements (MITC6). The normalized shell thickness is (a) $t/R = 10^{-2}$ and (b) $t/R = 10^{-3}$.

Table 3: Exact solution of the strain energy for the free cylinder problem, from [46]. The energy is $C \times \frac{6p_0R^3(1-\nu^2)}{E}\left(\frac{t}{R}\right)^3$.

t/R	C
0.01	0.704242080729323
0.001	0.700057056738260

$t/R = 10^{-3}$ case, the accuracy of the proposed method is poorer than the MITC elements for coarse meshes, but surpasses the MIT4 element by the third refinement level and reaches similar accuracy to the MITC6. An additional refinement level was performed with the present method to show that this level of accuracy is maintained. Again, the accuracy of the method remains acceptable in the thin limit. This benchmark and the previous one attest to the versatility of the method as a high performing tool in both asymptotic limits.

5.6. Scordelis-Lo roof

The Scordelis-Lo roof problem is a classic shell benchmark. It has been shown to be a problem of "intermediate" character in the thin limit, having finite bending and membrane energies as $t \to 0$ [48]. A cylindrical section is loaded by gravity. The boundary conditions are shown in Figure 11a; the rigid diaphragm condition is enforced as zero displacements in the x- and z-directions. The span angle is 80°, the roof length is 50 ft, the radius is 25 ft and the shell thickness is 0.25 ft. The material properties are $E = 432 \times 10^6$ lb/ft^2 and $\nu = 0$. The gravity load is 90 lb/ft^2 in the negative z-direction. Scordelis and Lo computed the vertical displacement of the mid-span at the free edge as 0.3024 ft, which is used to normalize the numerical results in Figure 11b. The current method is compared with a series of other shell elements: the MITC4 element, the DG method of Güzey et al. [27], the one-point quadrature degenerated solid shells of Liu et al. [52], and the assumed strain element of Simo et al. [53]. In this point-wise displacement metric, the present DG method converges rapidly and without overshoot.

6. Nonlinear benchmarks

In this section, benchmark problems with geometric and material nonlinearities are solved with the proposed method to assess its ability to function as a practical engineering tool.

6.1. Roll-up of a beam

This test is a classical elastica problem of Euler commonly used to demonstrate the large deformation capability of beam and shell elements. A flat cantilever beam of length L width w, and thickness t is subjected to a moment M at its tip. Euler's theory predicts that the beam should deform into a complete circle at a value of $M = 2\pi EI/L$, with $I = wt^3/12$ the second moment of the cross-sectional area. The parameters of the problem are indicated in Table 4.

The problem was solved in 12 equal load increments. Figure 12 depicts the equilibrium position of the beam at several load increments, as well as the final deformed shape. The convergence condition was set to be when the L^2 norm of the residual forces is reduced to 10^{-8} of the initial out-of-balance. At each load increment, 10 Newton iterations were required to reach equilibrium. The robsutness of the proposed method can be appreciated by comparing these results with the performance of the "S4R" element of the commercial finite element code Abaqus. In fact, Sze et al. [54] report a much larger number of load steps (125) and maximum permitted number of Newton iterations (714) convergence using the default convergence criteria and the default adaptive load incrementing scheme on the same problem.

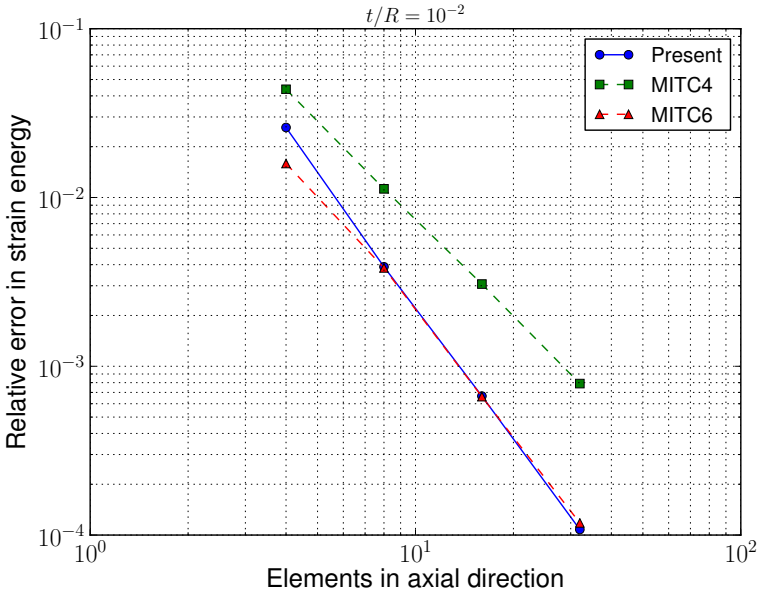

(a)

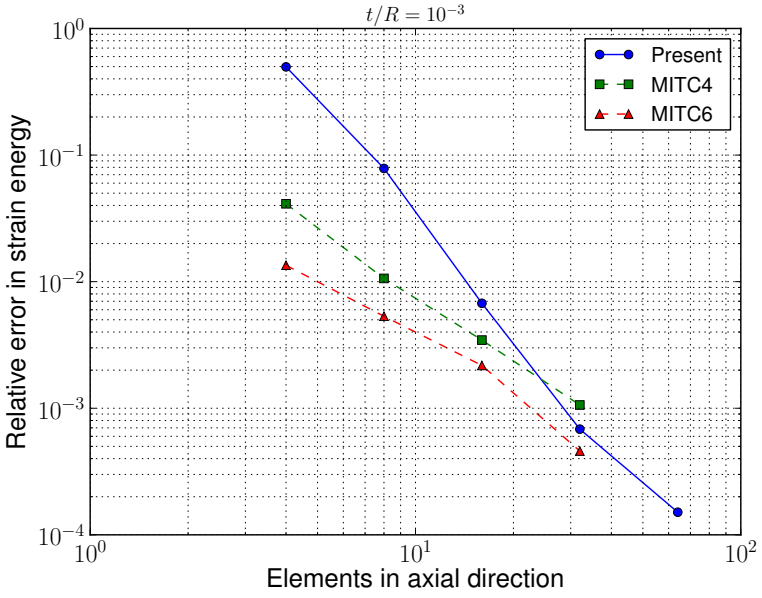

(b)

Figure 10: Relative error of the strain energy in the free cylinder benchmark. Results plotted for current DG scheme as well as quadrilateral first order MITC elements (MITC4) and triangular second order MITC elements (MITC6). The normalized shell thickness is (a) $t/R = 10^{-2}$ and (b) $t/R = 10^{-3}$.

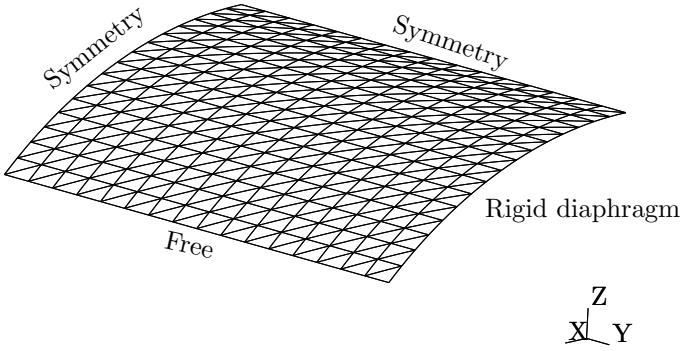

(a)

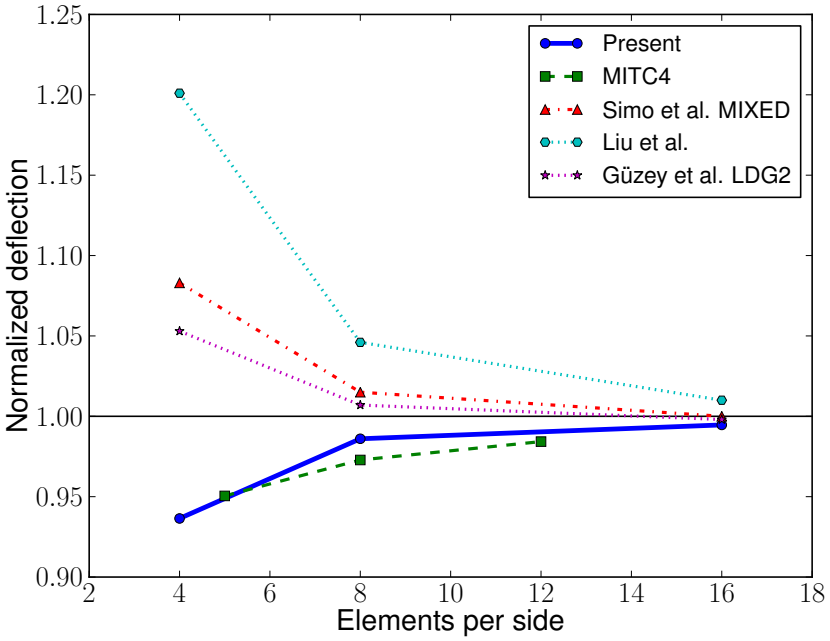

(b)

Figure 11: (a) Mesh and boundary conditions of the Scordelis-Lo roof problem. (b) Numerical calculations of the Scordelis-Lo roof benchmark compared with selected other formulations.

Table 4: Parameters used in the beam roll-up problem.

Parameter	Value
E	12×10^6 Pa
ν	0
L	10 m
w	1 m
t	0.1 m
c_x	5
c_T	5

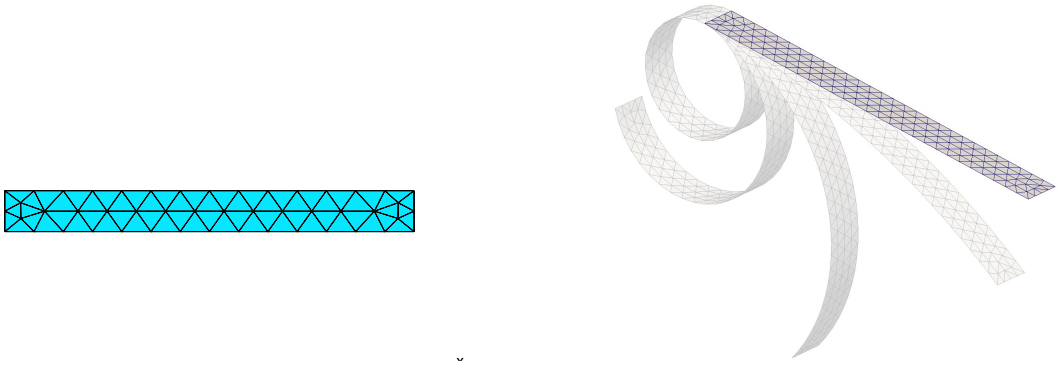

(a) (b)

Figure 12: Mesh and results for the clamped beam roll-up problem. (a) Mesh (b) the undeformed configuration and the equilibrium position found after several of the loading increments, including the final state.

6.2. Twisting of a bar

A cantilevered bar of length L, width w, and thickness t is twisted by application of a torque T at the free end. This is another test of the shell method to efficiently find equilibrium positions under large deformations and rotations. The parameters of the problem are given in Table 5. Note that in this case, the bar is rather thick, with $t/w = 0.2$. The in-plane dimensions of the bar are the same as the previous problem, and the same mesh is used. The material is taken to be elastic.

The load is applied in 25 equal increments. The convergence criterion is again taken to be a reduction in the L^2 norm of the residual to 10^{-8} of the value at the start of the load increment. The final state of the bar is shown in Figure 13. The deformation is clearly quite large, with the bar being subjected to approximately one and a half turns. The maximum number of Newton iterations needed in any increment is 8, and the median value is 5. In fact, the number of Newton iterations to reach equilibrium *decreased* as the total load increased. These features illustrate the robust convergence behavior obtained with the interpolations and exact update formulae. In the absence of an exact solution for comparison, this example was carried out for the sole purpose of showing the reliable performance of the quasi-static method in the presence of very large deformations.

6.3. Pinched open hemisphere

The pinched open hemisphere problem is commonly used as a benchmark for both linear and nonlinear shells. In this problem, a hemispherical shell with an 18° hole in the top is loaded by two pairs of diametrically opposed forces on the equator, separated by 90°. The forces are equal in magnitude, but opposite in sense (see Figure 14a). The parameters of the problem are given in Table 6.

Table 5: Parameters used for bar torsion problem.

Parameter	Value
E	12×10^6 Pa
ν	0
L	10 m
w	1 m
t	0.2 m
T	20×10^3 N m
c_x	5
c_T	5

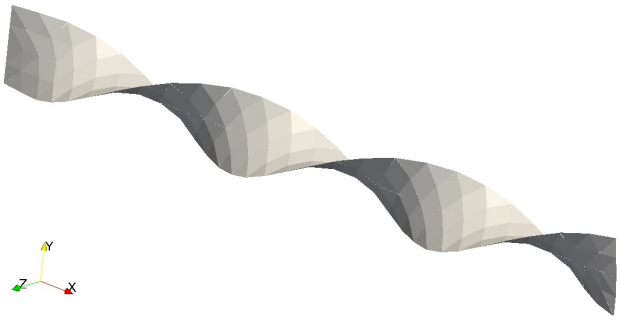

Figure 13: Final state of the bar in the torsion problem after twisting through one and a half turns.

Point loads are not admissible loads for shear-flexible shells with generalized Reissner-Mindlin kinematics, such as the theory used in this thesis. Hence, despite its popularity, the utility of this problem as a benchmark is limited. Yet, due to the fact that this example is so widely used, it is included here to show that the behavior of the proposed DG method behaves similarly to other accepted shell methods. The results are presented in Figure 14c as force vs. displacement plots of the inward and outward load points. The present method is compared with the shell element of Simo et al. [55], which is based on the same shell theory as the proposed method, but uses an assumed strain approach to control locking. Additionally, results are included from the standard shell element of the widely used commercial solid mechanics software Abaqus [56] (the Abaqus data come through the published work of Sze et al. [54]). The proposed method predicts very similar results to the both of the other element formulations. The geometric nonlinearity in this problem is rather strong, which may be observed from the disparity in the magnitudes of the inward and outward displacements.

Table 6: Parameters used in the pinched hemisphere problem.

Parameter	Value
E	68.25×10^6 Pa
ν	0.3
R	10 in
t	0.04 in

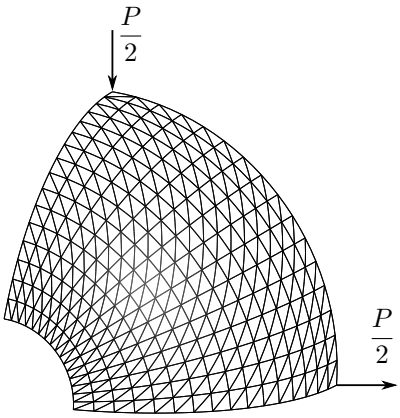

(a)

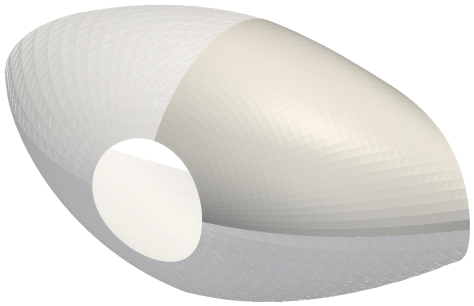

(b)

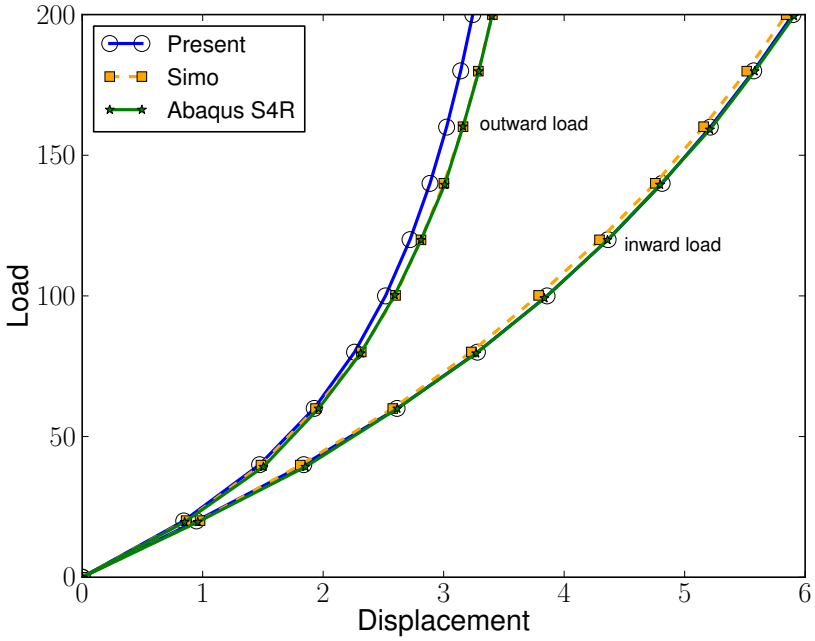

(c)

Figure 14: (a) Initial geometry of the pinched hemisphere problem showing the mesh. Quarter symmetry is exploited. (b) Deformed geometry at $P = 200$. (Results have been reflected across symmetry planes to depict entire domain.) (c) Force-displacement plots for the present method, as well as the shell element of Simo [55] and the "S4R" shell element in the commercial finite element code Abaqus [56].

6.4. Bending to membrane transition in a circular plate

The problem tests the ability of the proposed method to capture the nonlinear transition of a circular plate from bending to membrane behavior under large deflections. The problem setup is illustrated in 15a. A circular clamped plate is subjected to transverse distributed load and possible radial pre-tension. The clamped plate has radius a and thickness t, and is loaded quasi-statically with a spatially uniform transverse load of strength p_0 that increases in time. (The direction of the load remains fixed, perpendicular to the undeformed plate surface.) Additionally, a radial pre-tension with intensity N_0 is applied at the start of the simulation. The equilibrium position is found, then the external boundary is held fixed as the lateral load is increased. The Poisson's ratio of the material is $\nu = 0.27$. The independent variables in dimensionless form are $\frac{p_0 a^4}{Et^4}$, characterizing the transverse load intensity, and $k = \frac{a}{t}\sqrt{\frac{12(1-\nu^2)N_0}{Et}}$, characterizing the pre-tension. The plate aspect ratio t/a is taken as 0.1, so that the numerical results may be compared with calculations from thin plate theory. The response of the plate is measured in terms of w/a, the center point transverse deflection normalized by the radius.

Quarter symmetry is exploited in the mesh, which is shown in Figure 15b. The predicted response of the plate is shown in Figure 16 in terms of load intensity vs. transverse deflection of the plate center. The response of the plate is initially governed by bending and can be described well with Kirchhoff plate theory, which predicts that the deflection scales linearly with p_0. As the deflection of the plate grows to be comparable with the thickness, membrane effects become important, and the response becomes increasingly nonlinear. At large deflections, bending effects are small, and the plate response is dominated by in-plane membrane forces, and membrane theory predicts that the transverse displacement goes as $\sim p_0^{1/3}$. Simulations are conducted for three levels of pre-tension, and are compared with semi-analytical [7] predictions of Sheplak and Dugundji using von Kármán nonlinear plate theory [57]. The results are plotted on logarithmic scales so that the asymptotic behaviors can be clearly seen. The proposed method closely reproduces the published results. It is particularly noteworthy that the proposed method accurately captures the transition with a rather coarse mesh. (There is a boundary layer in the solution near the clamped boundary, resolving this would improve the results further). The bending to membrane transition is present in many technologically important fracture problems involving impact and penetration, such as the design of force protection and armor systems, and ship grounding analysis in naval architecture.

7. Summary and Conclusions

A discontinuous Galerkin method was proposed for the analysis of finitely deforming, shear-flexible shells. The key feature of this method is that the usual tools to prevent locking in shells, mixed formulations and reduced integration, are eschewed in favor of a selection of approximation spaces that are compatible with the thin shell limit. Numerical evidence was presented that suggests the method is accurate and locking-free. As in most discontinuous Galerkin methods, the number of unknowns generated for a given mesh is higher than competing conforming methods; on the other hand, the absence of mixed variables allows the proposed method to be cast variationally, in terms of an energy minimum principle. The energy principle approach could prove advantageous for solution methods and mesh adaptation.

Acknowledgements

This research was supported by the U.S. Army through the Institute for Soldier Nanotechnologies, under contract DAAD-19-02-D-0002 with the U.S. Army Research Office, and by the Office of Naval Research (ONR grant number N00014-07-1-0764) as part of a Multidisciplinary University Research Initiative (David Shifler, Program Manager). The content does not necessarily reflect the position of the government, and no official endorsement should be inferred. The authors thank Mr. Gauthier Becker for help with the

[7] Sheplak and Dugundji reduce the problem to one dimension using axisymmetry, and then numerically solve the resulting ordinary differential equation with a finite difference method.

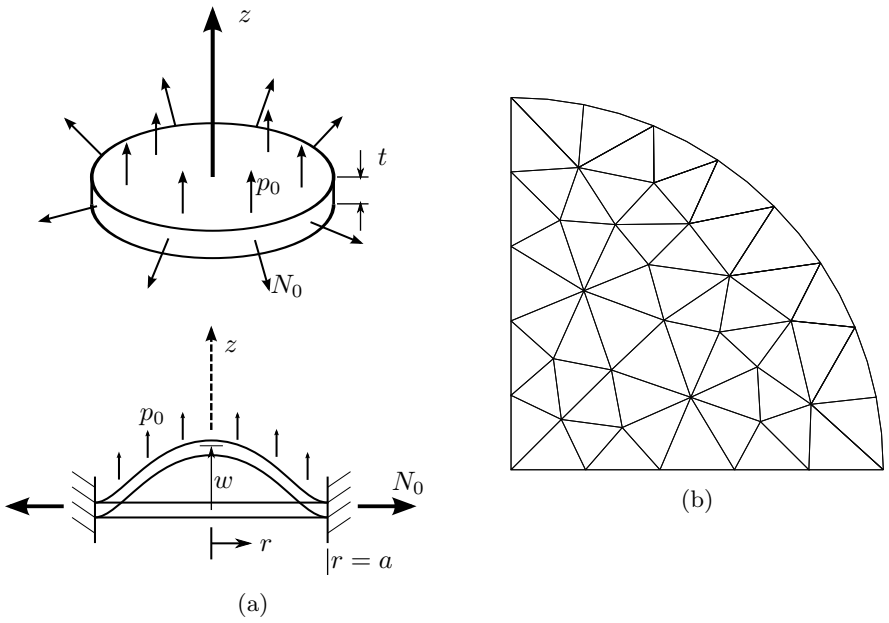

Figure 15: (a) Schematic of the clamped circular plate problem. (b) Mesh used in simulation showing quarter symmetry.

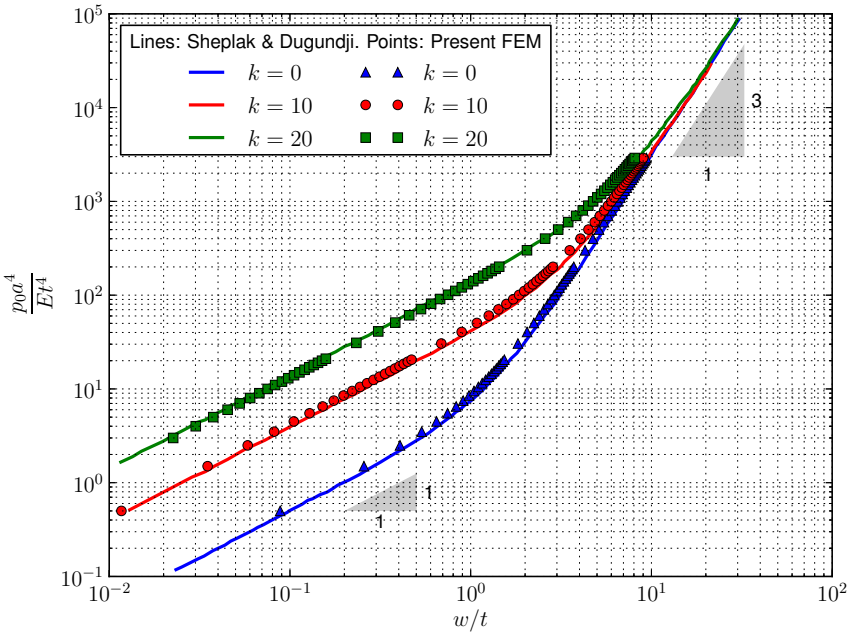

Figure 16: Clamped circular plate under uniform pressure benchmark problem. Normalized pressure vs. center point deflection. Solid lines are data from 1D finite difference calculations of Dugundji and Sheplak [57] using von Kármán plate theory. Discrete points are the present DG shell element. The dimensionless parameter $k = \frac{a}{t}\sqrt{\frac{12(1-\nu^2)N_0}{Et}}$ characterizes the pre-tension.

implementation and in particular for his adroit programming with `Gmsh`. Additionally, BT acknowledges the Progetto Roberto Rocca for fellowship support for a research stay of a semester at the Politecnico di Milano.

Appendix A. Stiffness matrices

Appendix A.1. Bulk element stiffness matrix

The material and geometric parts involve areal integrals, and thus lead to the bulk element stiffness matrix $[\mathbf{k}]$,

$$[\mathbf{k}] = [\mathbf{k}^{\mathrm{M}}] + [\mathbf{k}^{\mathrm{G}}]$$

The material part of the stiffness matrix can be partitioned according to the fields as in

$$[\mathbf{k}^{\mathrm{M}}] = \begin{bmatrix} [\mathbf{k}^{\mathrm{M}}_{xx}] & [\mathbf{k}^{\mathrm{M}}_{xT}] \\ [\mathbf{k}^{\mathrm{M}}_{Tx}] & [\mathbf{k}^{\mathrm{M}}_{TT}] \end{bmatrix} \tag{A.1}$$

The submatrices are

$$[\mathbf{k}^{\mathrm{M}}_{xx}]^{AB} = \int_{\hat{E}} \left(\partial_\alpha N^A \pm \sum_{e=1}^{3} [r^e]^A_\alpha\right)\left(\partial_\gamma N^B \pm \sum_{e=1}^{3} [r^e]^B_\gamma\right)\Big(H^{\alpha\beta\gamma\delta}_{\mathrm{m}}\mathbf{a}_\beta \otimes \mathbf{a}_\delta + H^{\alpha\gamma}_{\mathrm{s}}\mathbf{t}_h \otimes \mathbf{t}_h + H^{\alpha\beta\gamma\delta}_{\mathrm{b}}\mathbf{b}_\beta \otimes \mathbf{b}_\delta\Big)\bar{j}\, d\mathcal{A} \tag{A.2}$$

$$[\mathbf{k}^{\mathrm{M}}_{xT}]^{AB} = \int_{\hat{E}} \left(\partial_\alpha N^A \pm \sum_{e=1}^{3} [r^e]^A_\alpha\right) L^B H^{\alpha\beta}_{\mathrm{s}}\mathbf{t}_h \otimes (\bar{\mathbf{\Lambda}}^\top_B \mathbf{a}_\beta)\bar{j}\, d\mathcal{A} + \int_{\hat{E}} \left[\left(\partial_\alpha N^A \pm \sum_{e=1}^{3} [r^e]^A_\alpha\right)\left(\partial_\delta L^B \pm \sum_{e=1}^{3} [\mathsf{r}^e]^B_\delta\right) H^{\alpha\beta\gamma\delta}_{\mathrm{b}}\mathbf{b}_\beta \otimes (\bar{\mathbf{\Lambda}}^\top_B \mathbf{a}_\gamma)\right]\bar{j}\, d\mathcal{A} \tag{A.3}$$

$$[\mathbf{k}^{\mathrm{M}}_{TT}]^{AB} = \int_{\hat{E}} \left(\partial_\beta L^A \pm \sum_{e=1}^{3} [\mathsf{r}^e]^A_\beta\right)\left(\partial_\delta L^B \pm \sum_{e=1}^{3} [\mathsf{r}^e]^B_\delta\right) H^{\alpha\beta\gamma\delta}_{\mathrm{b}}(\bar{\mathbf{\Lambda}}^\top_A \mathbf{a}_\alpha) \otimes (\bar{\mathbf{\Lambda}}^\top_B \mathbf{a}_\gamma)\bar{j}\, d\mathcal{A} + \int_{\hat{E}} L^A L^B \otimes H^{\alpha\beta}_{\mathrm{s}}(\bar{\mathbf{\Lambda}}^\top \mathbf{a}_\alpha) \otimes (\bar{\mathbf{\Lambda}}^\top_B \mathbf{a}_\beta)\bar{j} d\mathcal{A} \tag{A.4}$$

and $[\mathbf{k}^{\mathrm{M}}_{Tx}] = [\mathbf{k}^{\mathrm{M}}_{Tx}]^\top$.

The geometric part of the stiffness matrix is likewise partitioned according to the fields, giving

$$[\mathbf{k}^{\mathrm{G}}] = \begin{bmatrix} [\mathbf{k}^{\mathrm{G}}_{xx}] & [\mathbf{k}^{\mathrm{G}}_{xT}] \\ [\mathbf{k}^{\mathrm{G}}_{Tx}] & [\mathbf{0}] \end{bmatrix}$$

with the submatrices given by

$$[\mathbf{k}^{\mathrm{G}}_{xx}]^{AB} = \int_{\hat{E}} \widetilde{n}^{\alpha\beta}\left(\partial_\alpha N^A \pm \sum_{e=1}^{3} [r^e]^A_\alpha\right)\left(\partial_\beta N^B \pm \sum_{e=1}^{3} [r^e]^B_\beta\right)\mathbf{1}\bar{j}\, d\mathcal{A} \tag{A.5}$$

$$[\mathbf{k}^{\mathrm{G}}_{xT}]^{AB} = \int_{\hat{E}} \widetilde{q}^{\alpha} L^A \left(\partial_\alpha N^B \pm \sum_{e=1}^{3} [r^e]^B_\alpha \right) \bar{\mathbf{\Lambda}}_A \bar{j}\, d\mathcal{A} + \int_{\hat{E}} \widetilde{m}^{\beta\alpha} \left(\partial_\alpha L^A \pm \sum_{e=1}^{3} [\mathbf{r}^e]^A_\alpha \right) \left(\partial_\beta N^B \pm \sum_{e=1}^{3} [r^e]^B_\beta \right) \bar{\mathbf{\Lambda}}_A \bar{j}\, d\mathcal{A} \quad \text{(A.6)}$$

where $\mathbf{1}$ is the three-dimensional identity tensor, and $[\mathbf{k}^{\mathrm{G}}_{Tx}] = [\mathbf{k}^{\mathrm{G}}_{xT}]^\top$.

Appendix A.2. Stability interface element stiffness matrix

The stability terms are computed on the interface elements with the integrals

$$[\mathbf{k}^e_{\mathrm{xx,stab}}]^{AB} = \pm \int_e \frac{\beta_x}{h_e} N^A N^B \bar{j}^0 ds \quad \text{(A.7)}$$

$$[\mathbf{k}^e_{\mathrm{TT,stab}}]^{AB} = \pm \int_e \frac{\beta_T}{h_e} L^A L^B (\bar{\mathbf{\Lambda}}^A)^\top \bar{\mathbf{\Lambda}}^B \bar{j}^0 ds \quad \text{(A.8)}$$

The positive sign applies when both shape functions are from the same side of the interface, and the negative sign applies otherwise. The interface element stiffness matrix is then

$$[\mathbf{k}^e_{\mathrm{stab}}] = \begin{bmatrix} [\mathbf{k}^e_{\mathrm{xx,stab}}] & \mathbf{0} \\ \mathbf{0} & [\mathbf{k}^e_{\mathrm{TT,stab}}] \end{bmatrix}$$

[1] Richard S. Falk. Finite elements for the Reissner-Mindlin plate. In Daniele Boffi and Lucia Gastaldi, editors, *Mixed Finite Elements, Compatibility Conditions, and Applications*, Lecture Notes in Mathematics, pages 195–232. Springer-Verlag, Berlin Heidelberg, 2008.

[2] Richard H. Macneal. Derivation of element stiffness matrices by assumed strain distributions. *Nuclear Engineering and Design*, 70(1):3–12, 1982.

[3] K.J. Bathe and N. Dvorkin. A four-node plate bending element based on Mindlin/Reissner plate theory and a mixed interpolation. *International Journal for Numerical Methods in Engineering*, 21:367–383, 1985.

[4] D.N. Arnold and R.S. Falk. A uniformly accurate finite element method for the Reissner-Mindlin plate. *SIAM Journal of Numerical Analysis*, 26:1276–1290, 1989.

[5] Franco Brezzi, Klaus-Jürgen Bathe, and Michel Fortin. Mixed-interpolated elements for Reissner–Mindlin plates. *International Journal for Numerical Methods in Engineering*, 28(8):1787–1801, 1989.

[6] Franco Brezzi, Michel Fortin, and Rolf Sternberg. Error analysis of mixed-interpolated elements for Reissner-Mindlin plates. *Mathematical Models and Methods in Applied Sciences*, 01(02):125–151, 1991.

[7] Eduardo N. Dvorkin and Klaus-Jürgen Bathe. A continuum-mechanics based four-node shell element for general non-linear analysis. *Engineering Computations*, 1:77–98, 1984.

[8] K.J. Bathe and N. Dvorkin. A formulation of general shell elements - the use of mixed interpolation of tensorial components. *International Journal for Numerical Methods in Engineering*, 22:697–722, 1986.

[9] M.L. Bucalem and J. Bathe. Higher-order MITC general shell elements. *International Journal for Numerical Methods in Engineering*, 36:3729–3754, 1993.

[10] Thomas J.R. Hughes, Martin Cohen, and Medhat Haroun. Reduced and selective integration techniques in the finite element analysis of plates. *Nuclear Engineering and Design*, 46(1):203–222, 1978.

[11] Thomas J.R. Hughes and Wing Kam Liu. Nonlinear finite element analysis of shells: Part I. three-dimensional shells. *Computer Methods in Applied Mechanics and Engineering*, 26(3):331 – 362, 1981.

[12] Thomas J.R. Hughes. *The finite element method: Linear static and dynamic finite element analysis*. Dover Publications, Inc, New York, 2000.

[13] Ted Belytschko and Chen-Shyh Tsay. A stabilization procedure for the quadrilateral plate element with one-point quadrature. *International Journal for Numerical Methods in Engineering*, 19(3):405–419, 1983.

[14] T. Belytschko and I. Leviathan. Physical stabilization of the 4-node shell element with one point quadrature. *Computer Methods in Applied Mechanics and Engineering*, 113:321–350, 1994.

[15] Q. Zeng and A. Combescure. A new one-point quadrature, general non-linear quadrilateral shell element with physical stabilization. *International Journal for Numerical Methods in Engineering*, 42:1307–1338, 1998.

[16] Franco Brezzi and Klaus-Jürgen Bathe. A discourse on the stability conditions for mixed finite element formulations. *Computer Methods in Applied Mechanics and Engineering*, 82:27–57, 1990.

[17] F. Brezzi and M. Fortin. *Mixed and Hybrid Finite Element Methods*. Springer, Berlin, 1991.

[18] David S. Malkus and Thomas J. R. Hughes. Mixed finite element methods – reduced and selective integration techniques: a unification of concepts. *Computer Methods in Applied Mechanics and Engineering*, 15(1):63–81, 1978.

[19] P. Hansbo and M.G. Larson. Discontinuous Galerkin methods for incompressible and nearly incompressible elasticity by Nitsche's method. *Computer Methods in Applied Mechanics and Engineering*, 191:1895–1908, 2002.

[20] A. Ten Eyck and A. Lew. Discontinuous Galerkin methods for nonlinear elasticity. *International Journal for Numerical Methods in Engineering*, 67:1204–1243, 2006.
[21] Yongxing Shen and Adrian J Lew. A family of discontinuous Galerkin mixed methods for nearly and perfectly incompressible elasticity. *ESAIM: Mathematical Modelling and Numerical Analysis*, 46(05):1003–1028, 2012.
[22] B. Cockburn, G. Kanschat, D. Schötzau, and C. Schwab. Local discontinuous Galerkin methods for the Stokes system. *SIAM Journal on Numerical Analysis*, 40(1):319–343, 2002.
[23] D.N. Arnold, F. Brezzi, and L. D. Marini. A family of discontinuous Galerkin finite elements for the Reissner-Mindlin plate. *Journal of Scientific Computing*, 22-23:25–45, 2005.
[24] D.N. Arnold, F. Brezzi, R. S. Falk, and L. D. Marini. Locking free Reissner-Mindlin elements without reduced integration. *Computer Methods in Applied Mechanics and Engineering*, 196:3660–3671, 2006.
[25] Paulo R. Bösing, Alexandre L. Madureira, and Igor Mozolevski. A new interior penalty discontinuous Galerkin method for the Reissner–Mindlin model. *Mathematical Models and Methods in Applied Sciences*, 20(08):1343–1361, August 2010.
[26] Peter Hansbo, David Heintz, and Mats G. Larson. A finite element method with discontinuous rotations for the Mindlin-Reissner plate model. *Computer Methods in Applied Mechanics and Engineering*, 200(5-8):638–648, January 2011.
[27] S. Güzey, H.K. Stolarski, B. Cockburn, and K.K. Tamma. Design and development of a discontinuous Galerkin method for shells. *Computer Methods in Applied Mechanics and Engineering*, 195:3528–3548, 2006.
[28] S. Güzey, B. Cockburn, and H.K. Stolarski. The embedded discontinuous Galerkin method: Application to linear shell problems. *International Journal for Numerical Methods in Engineering*, 2007.
[29] A. Lew, P. Neff, D. Sulsky, and M. Ortiz. Optimal BV estimates for a discontinuous Galerkin method for linear elasticity. *Applied Mathematics Research eXpress*, 3:73–106, 2004.
[30] L. Noels and R. Radovitzky. A general discontinuous Galerkin method for finite hyperelasticity. Formulation and numerical applications. *International Journal for Numerical Methods in Engineering*, 68(1):64–97, 2006.
[31] R. Radovitzky and M. Ortiz. Error estimation and adaptive meshing in strongly nonlinear dynamic problems. *Computer Methods in Applied Mechanics and Engineering*, 172:203–240, 1999.
[32] P Thoutireddy and M Ortiz. A variational r-adaption and shape-optimization method for finite-deformation elasticity. *International Journal for Numerical Methods in Engineering*, 61(1):1–21, 2004.
[33] J. Mosler and M. Ortiz. Variational h-adaption in finite deformation elasticity and plasticity. *International Journal for Numerical Methods in Engineering*, 72:505–523, 2007.
[34] J.C. Simo and D.D. Fox. On a stress resultant geometrically exact shell model. Part I: formulation and optimal parametrization. *Computer Methods in Applied Mechanics and Engineering*, 72:267–304, 1989.
[35] J.C. Simo. On a stress resultant geometrically exact shell model. Part VII: shell intersections with 5/6-dof finite element formulations. *Computer Methods in Applied Mechanics and Engineering*, 108:319–339, 1993.
[36] J.C. Simo, D.D. Fox, and M.S. Rifai. On a stress resultant geometrically exact shell model. Part III: computational aspects of the non-linear theory. *Computer Methods in Applied Mechanics and Engineering*, 79:21–70, 1990.
[37] D.N. Arnold, F. Brezzi, B. Cockburn, and L.D. Marini. Unified analysis of discontinuous Galerkin methods for elliptic problems. *SIAM Journal on Numerical Analysis*, 39(5):1749–1779, 2002.
[38] M. Ortiz and L. Stainier. The variational formulation of viscoplastic updates. *Computer Methods in Applied Mechanics and Engineering*, 171:419–444, 1999.
[39] C. Geuzaine and J.-F. Remacle. Gmsh: a three-dimensional finite element mesh generator with built-in pre- and post-processing facilities. *International Journal for Numerical Methods in Engineering*, 79(11):1309–1331, 2009.
[40] F. Cirak, M. Ortiz, and P. Schröder. Subdivision surfaces: a new paradigm for thin-shell finite-element analysis. *International Journal for Numerical Methods in Engineering*, 47:2039–2072, 2000.
[41] F. Cirak and M. Ortiz. Fully C^1-conforming subdivision elements for finite deformation thin-shell analysis. *International Journal for Numerical Methods in Engineering*, 51:813–833, 2001.
[42] Q. Long, P. B. Bornemann, and F. Cirak. Shear-flexible subdivision shells. *International Journal for Numerical Methods in Engineering*, 90:1549–1577, 2012.
[43] P.-O. Persson and J. Peraire. Newton-GMRES preconditioning for discontinuous Galerkin discretizations of the navier-stokes equations. *SIAM Journal on Scientific Computing*, 30(6):2709–2733, 2008.
[44] Satish Balay, Jed Brown, Kris Buschelman, Victor Eijkhout, William D. Gropp, Dinesh Kaushik, Matthew G. Knepley, Lois Curfman McInnes, Barry F. Smith, and Hong Zhang. PETSc users manual. Technical Report ANL-95/11 - Revision 3.1, Argonne National Laboratory, 2010.
[45] Alex Ten Eyck, Fatih Celiker, and Adrian Lew. Adaptive stabilization of discontinuous Galerkin methods for nonlinear elasticity: Motivation, formulation, and numerical examples. *Computer Methods in Applied Mechanics and Engineering*, 197:45–48, 2008.
[46] J. Pitkäranta, Y. Leino, O. Ovaskainen, and J. Piila. Shell deformation states and the finite element method: A benchmark study of cylindrical shells. *Computer Methods in Applied Mechanics and Engineering*, 128:81–121, 1995.
[47] M. Malinen and J. Pitkäranta. A benchmark study of reduced-strain shell finite elements: quadratic schemes. *International Journal for Numerical Methods in Engineering*, 48:1637–1671, 2000.
[48] D. Chapelle and K. J. Bathe. Fundamental considerations for the finite element analysis of shell structures. *Computer & Structures*, 66:19–36, 1998.
[49] K. J. Bathe, A. Iosilevich, and D. Chapelle. An evaluation of the MITC shell elements. *Computer & Structures*, 75:1–30, 2000.
[50] Dominique Chapelle and Klaus-Jürgen Bathe. *The finite element analysis of shells – fundamentals*. Computational Fluid and Solid Mechanics. Springer, second edition, 2010.
[51] C Chinosi and C Lovadina. Numerical analysis of some mixed finite element methods for Reissner-Mindlin plates. *Com-*

putational Mechanics, 16(1):36–44, 1995.
[52] K.K. Liu, E.S. Law, D. Lam, and T. Belytschko. Resultant-stress degenerated shell element. *Computer Methods in Applied Mechanics and Engineering*, 55:259–300, 1986.
[53] J.C. Simo, D.D. Fox, and M.S. Rifai. On a stress resultant geometrically exact shell model. Part II: the linear theory; computational aspects. *Computer Methods in Applied Mechanics and Engineering*, 73:53–92, 1989.
[54] K.Y. Sze, X.H. Liu, and S.H. Lo. Popular benchmark problems for geometric nonlinear analysis of shells. *Finite Elements in Analysis and Design*, 40:1551–1569, 2004.
[55] J.C. Simo and J.G. Kennedy. On a stress resultant geometrically exact shell model. Part V: Nonlinear plasticity: formulation and integration algorithms. *Computer Methods in Applied Mechanics and Engineering*, 96:133–171, 1992.
[56] Dassault Systèmes Simulia Corp., Providence, RI. *Abaqus: User's Manual and Theory Manual*, version 6.11 edition, 2011.
[57] M. Sheplak and J. Dugundji. Large deflections of clamped circular plates under initial tension and transitions to membrane behavior. *Journal of Applied Mechanics*, 65:107–115, March 1998.
[58] J.S. Hesthaven. From electrostatics to almost optimal nodal sets for polynomial interpolation in a simplex. *SIAM Journal on Numerical Analysis*, 35:655–676, 1998.
[59] J.S. Hesthaven and T. Warburton. Nodal high-order methods on unstructured grids. *Journal of Computational Physics*, 181:186–221, September 2002.
[60] M.A. Taylor, B.A. Wingate, and R.E. Vincent. An algorithm for computing Fekete points in the triangle. *SIAM Journal of Numerical Analysis*, 38(5):1707–1720, 2000.